Electronic Supplementary Material (ESI) for Journal of Materials Chemistry C.

Supporting information

The Role of Dinuclearity in Promoting Thermally Activated Delayed Fluorescence (TADF) in Cyclometallated, N^C^N-coordinated Platinum(II) Complexes

Piotr Pander, Andrey V. Zaytsev, Amit Sil, J. A. Gareth Williams, Pierre-Henri Lanoe, Valery N. Kozhevnikov and Fernando B. Dias

Table of contents

1. General

Theory

To assist the interpretation of the experimental results, we have performed density functional theory (DFT) and time-dependent density functional theory (TDDFT) simulations with Tamm-Dancoff approximation (TDA) on the di- and mononuclear complexes using the ORCA 4.2.1 quantum chemistry software[1–3]. All molecular orbital (MO) iso surfaces were visualised using Gabedit 2.5.0.[4]

Calculations were performed at different levels of theory:

- for the results in the ground state (S_0) geometry presented in the main text and within the supporting information (referred to as **B3LYP/def2-TZVP/ZORA** in the SI);
- for results in the supporting information in the ground (S_0) and triplet excited (T_1) state (referred to as **B3LYP/def2-SVP** in the SI).

The use of different levels of theory is justified by extensive calculation time of performing excited state geometry optimization using the triple-zeta def2-TZVP[5] basis set and instead a simpler split valence basis set def2-SVP[5] was used for excited state geometry optimization. All simulations were performed using the popular B3LYP[6,7] density functional. Where indicated, conductor-like polarizable continuum model for CH_2Cl_2 or toluene was used with the exception of the excited state T_1 geometry which was optimized in a vacuum. Ground and excited state geometries were verified to be true energy minima by a frequency calculation. All optimisations were performed with tight SCF and geometry optimisation criteria.

B3LYP/def2-TZVP/ZORA (main text and SI where indicated). A triple-zeta def2-TZVP basis set with the def2/J[8] auxiliary basis set were used for all atoms for an accurate assessment of the ground state geometry S_0 of the mono- and the di-Pt(II) complex. Excited state energy of TDDFT states was calculated using the resulting S_0 geometry. In this case relativistically corrected triple-zeta basis sets with the zeroth-order regular approximation (ZORA)[9,10] were used: ZORA-def2-TZVP[5] with the SARC/J[11] auxiliary basis for all atoms except Pt where a segmented all-electron relativistically contracted (SARC) SARC-ZORA-TZVP[11] basis set was used. Spin-orbit coupling (SOC) calculations were performed as implemented in the ORCA software. SOC matrix elements (SOCME) and SOC-corrected excitations (SOC-TDDFT states) were computed at the same level of theory as the TDDFT states. In order to accelerate the calculations a RIJCOSX[12,13] approximation was used in all cases and the RI-SOMF(1X) setting was used to accelerate SOC calculations. All computations were performed using a dense grid (Grid6, GridX6).

B3LYP/def2-SVP (calculations in the SI only). Owing to the smaller size of the split valence def2-SVP basis set as compared to the def2-TZVP basis the former offers a significant acceleration of the calculation, saving computation time. The def2-SVP basis set was used to optimise the ground state (S_0) and triplet excited triplet state geometries (T_1) and to obtain excited state energy at these geometries.

Calculation of singlet and triplet radiative rates using simulated parameters

Relationship between transition oscillator strength and radiative rate is described by[14]:

$$k_r = \frac{n^2 \nu^2 f}{1.5}$$

Where k_r – radiative rate of a given transition, s^{-1}; n – refractive index of the medium; ν – energy of the state represented as a wavenumber, cm^{-1}; f – transition oscillator strength.

Obtaining k_r of a singlet state is therefore straightforward. In order to obtain radiative phosphorescence rate we consider the thermal equilibrium between the three triplet substates as set out earlier by Mori and others[15]:

$$k_r^{av} = \frac{k_r^1 + k_r^2 e^{-\frac{\Delta E_{1,2}}{k_b T}} + k_r^3 e^{-\frac{\Delta E_{1,3}}{k_b T}}}{1 + e^{-\frac{\Delta E_{1,2}}{k_b T}} + e^{-\frac{\Delta E_{1,3}}{k_b T}}}$$

Where: k_r^{av} – average radiative rate, s^{-1}; k_r^1, k_r^2, k_r^3 – radiative rates of the SOC-TDDFT states 1-3, s^{-1}; k_b – Boltzmann constant, 8.617×10^{-5} eV K^{-1}; $\Delta E_{1,2}$ – energy difference between SOC-TDDFT states 1 and 2, eV; $\Delta E_{1,3}$ – energy difference between SOC-TDDFT states 1 and 3, eV; T – temperature, K.

In the calculation of the average triplet radiative rate we consider the thermal equilibrium at 295 K for comparison with experimental radiative rates obtained at room temperature.

Electrochemistry

Cyclic voltammetry was conducted in a three-electrode, one-compartment cell. All measurements were performed using 0.1 M Bu_4NBF_4 (99%, Sigma Aldrich, dried) solution in dichloromethane (ExtraDry AcroSeal®, Acros Organics). All solutions were purged with nitrogen prior to measurement and the measurement was conducted in a nitrogen atmosphere. Electrodes used: working (Pt disc d = 1 mm), counter (Pt wire), reference (Ag/AgCl calibrated against ferrocene). All cyclic voltammetry measurements were performed at room temperature with a scan rate of 50 mV s^{-1}.

The ionization potential (IP) and electron affinity (EA) are obtained from onset redox potentials; these figures correspond to HOMO and LUMO values, respectively. The ionization potential is calculated from onset oxidation potential $IP = E_{ox}^{CV} + 5.1$ and the electron affinity is calculated from onset reduction potential $EA = E_{red}^{CV} + 5.1$.[16],[17],[18],[19] An uncertainty of ±0.02 V is assumed for the electrochemical onset potentials.

Photophysics

Absorption spectra of 10^{-5} M solutions were recorded with UV-3600 double beam spectrophotometer (Shimadzu). Photoluminescence (PL) spectra of solutions and films were recorded using a QePro compact spectrometer (Ocean Optics) or FluoroLog fluorescence spectrometer (Jobin Yvon). Phosphorescence decays in film were recorded using nanosecond gated luminescence and lifetime measurements (from 400 ps to 1 s) using the third harmonic of a high-energy pulsed Nd:YAG laser emitting at 355 nm (EKSPLA). The emitted light was focused onto a spectrograph and detected with a sensitive gated iCCD camera (Stanford Computer Optics) having sub-nanosecond resolution. Time-resolved measurements were performed by exponentially increasing gate and integration times. Further details are available in reference[20]. Time-resolved decays in solution were recorded with a Horiba DeltaFlex TCSPC system using a 330 nm SpectraLED light source. Temperature-dependent experiments were conducted using a liquid nitrogen cryostat VNF-100 (sample in flowing vapour, Janis Research) under nitrogen atmosphere, while measurements at room temperature were recorded under vacuum in the same cryostat. Solutions were degassed using five freeze-pump-thaw cycles. Thin films in polystyrene and pristine layers were deposited from chloroform solutions. The films were fabricated through spin-coating and dried under vacuum at room temperature. Solid state emission spectra and photoluminescence quantum yield were obtained using an integrating sphere (Labsphere) coupled with a 365 nm LED light source and QePro (Ocean Optics) detector.

Photoluminescence measurements at temperatures above 300K

High temperature measurements were conducted in a closed cell in a solution deoxygenated by bubbling argon for 20 minutes. The cell was submerged in a stirred water bath with temperature

control. Optical steady-state and time-resolved measurements were conducted through the transparent walls of the bath.

Deconvolution of dual emission spectra to determine TADF-to-phosphorescence ratios

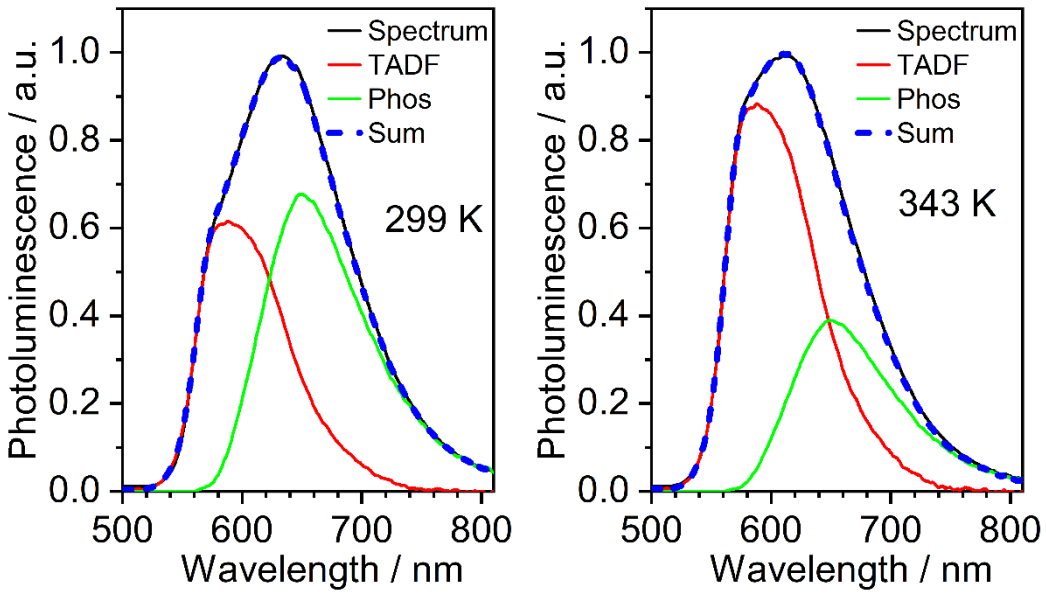

Figure S1.1. Deconvolution of photoluminescence spectrum of **2** in chlorobenzene, examples.

We are able to deconvolute the photoluminescence spectrum of **2** in chlorobenzene and toluene using the assumption that the two luminescent bands: TADF and phosphorescence do not change their shape with temperature, but temperature affects their proportion in the spectrum. We select two arbitrarily chosen spectra recorded at different temperatures and subtract one from another in order to obtain TADF spectrum as a product. We then subtract hence obtained TADF spectrum from a chosen experimental spectrum to obtain the phosphorescence spectrum. In the two subtractions we re-scale one spectrum in respect to the other in order to cancel out the contributions of the band that is not intended to appear in the product. Once obtained, TADF and phosphorescence spectra are used to fit every experimental spectrum and we can demonstrate that each spectrum can be presented as a sum of TADF and phosphorescence bands (**Figure S1.1**). This confirms the initial assumptions of the TADF and phosphorescence spectrum not changing shape with temperature was correct.

Once a photoluminescence spectrum at given temperature is fitted with the sum of TADF and phosphorescence the ratio between the bands can be obtained from the area under each of the individual components.

Determination of photoluminescence quantum yields in solution

Photoluminescence quantum yields were obtained using a gradient method in which we study relation (gradient) between total photoluminescence intensity and absorbance at excitation wavelength (same for both standard and analyte) in a range of concentrations for both analyte and standard – see equation below. We only consider data points with a constant gradient, so that the relation between photoluminescence and absorbance is linear – indication of the photoluminescence yield being independent of concentration in this region. The eligible concentration range was ~1-5 × 10^{-6} M in case of complexes **2** and **3** while absorbance of standards was kept at below 0.04 for Rhodamine 6G and 0.06 for Coumarine 153 at the respective excitation wavelengths.

$$\Phi_x = \Phi_{standard}\left(\frac{grad_x}{grad_{standard}}\right)\left(\frac{\eta_x^2}{\eta_{standard}^2}\right)$$

Where: Φ_x, $\Phi_{standard}$ – photoluminescence quantum yield of analyte and standard, respectively; $grad_x$, $grad_{standard}$- gradient (slope) of the linear relation between photoluminescence intensity and solution absorbance at the excitation wavelength, for analyte and standard, respectively; η_x , $\eta_{standard}$ - refractive index of solvent used for analyte and standard, respectively.

OLED devices

OLEDs were fabricated by spin-coating / evaporation hybrid method. The hole injection layer (PEDOT AL4083) and emitting layer (mCP:PO-T2T + dopant, or pristine) were spin-coated, whereas the electron transport layer (PO-T2T) and cathode (LiF/Al) were evaporated. Devices of 4 × 2mm pixel size were fabricated. 2,4,6-Tris[3-(diphenylphosphinyl)phenyl]-1,3,5-triazine (PO-T2T, sublimed, LUMTEC), 1,3-bis(carbazol-9-yl)benzene (mCP, sublimed, LUMTEC), LiF (99.995%, Sigma Aldrich), and Aluminium wire (99.9995%, Alfa Aesar) were purchased from the companies indicated in parentheses. OLED devices were fabricated using pre-cleaned with ozone plasma indium-tin-oxide (ITO) coated glass substrates with a sheet resistance of 20 Ω cm^{-2} and ITO thickness of 100 nm. PEDOT AL4083 was spun-coated and annealed onto a hotplate at 120 ˚C for 15 min to give a 30 nm film. Emitting layer was spun from chloroform:chlorobenzene (95:5 v/v) (10-20 mg/mL). The dopant was dissolved in the solution of blend host in order to obtain final 5-33% concentration in the emitting layer. All solutions were filtrated directly before application using a PVDF (organic solvents) and PES (PEDOT AL4083) syringe filter with 0.45 μm pore size. All other electron transport and cathode layers were thermally evaporated using Kurt J. Lesker Spectros II deposition system at 10^{-6} mbar base pressure. All organic materials and aluminium were deposited at a rate of 1 Å s^{-1}. The LiF layer was deposited at a rate of 0.1–0.2 Å s^{-1}. Characterisation of OLED devices was conducted in a 10 inch integrating sphere (Labsphere) connected to a Source Measure Unit and coupled with a spectrometer USB4000 (Ocean Optics). Further details are available in reference [21].

2. Synthesis

All solvents and reagents were purchased from commercial suppliers and used without further purification unless otherwise noted. NMR spectra were recorded on a JEOL ECS400FT Delta spectrometer (399.78 MHz for 1H NMR, 100.53 MHz for 13C NMR). Chemical shifts are reported in parts per million (ppm) relative to a tetramethylsilane internal standard. Elemental microanalysis was carried out at Durham University.

II

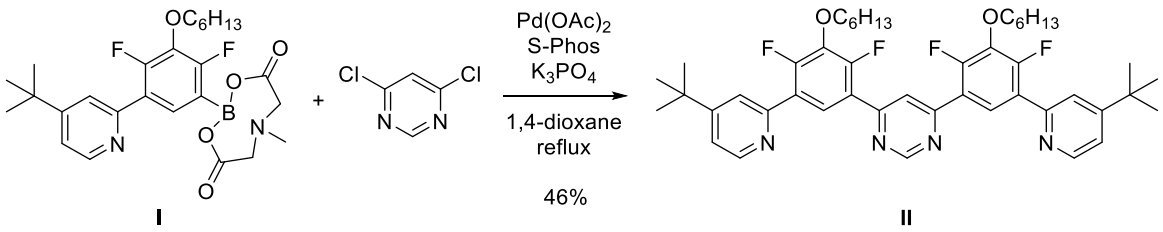

Potassium phosphate (4.66 g, 22 mmol, 5 eq.) was dissolved in water (10 mL) and the solution was deoxygenated by bubbling nitrogen through the mixture for 5 min. Dioxane (50 mL) was added and the mixture was further deoxygenated for 15 minutes. All other ingredients were combined as solids and added to the mixture. Deoxygenation was continued for additional 10 minutes. The mixture was submerged into oil bath which was pre-heated to 110°C. The mixture was heated under reflux for 12 hours. Upon cooling ethyl acetate (50 mL) and brine (50 mL) were added and the mixture was separated. The aqueous layer was washed with ethyl acetate. The combined organic phase was washed with brine and evaporated to dryness. The residue was treated with petrol ether to give solid. The solid was filtered off. The product was purified by column chromatography (silicagel, DCM/EA 2/1) to give the desired product as a colorless solid. Yield 750 mg (46%).

^{1}H NMR (400 MHz, $CDCl_3$) δ 9.37 (d, J = 1.2 Hz, 1H), 8.65 (d, J = 5.2 Hz, 2H), 8.42 (t, $^{4}J_{H\text{-}F}$ = 8.2 Hz, 2H), 8.28 (s, 1H), 7.73 (d, J = 2.0 Hz, 2H), 7.30 (dd, J = 5.2, 2.0 Hz, 2H), 4.25 (t, J = 6.6 Hz, 4H), 1.89 – 1.82 (m, 4H), 1.57 – 1.50 (m, 4H), 1.41 – 1.34 (m, 26H), 0.92 (app t, 6H).

^{13}C NMR (100 MHz, $CDCl_3$) δ 160.6 (quat.), 160.2 (quat.), 159.1 (CH), 156.7 (dd, J = 41.9 and 4.3 Hz, CF), 153.9 (dd, J = 42.2 and 4.9 Hz, CF), 152.2 (quat.), 149.8 (CH), 136.6 (t, J = 15.2 Hz, quat.), 125.7 (dd, J = 10.8 and 3.1 Hz, quat.), 125.6 (CH), 122.1 (dd, J = 9.5 and 3.4 Hz, quat.), 121.5 (d, J = 7.7 Hz, CH), 120.3 (t, J = 10.5 Hz, CH), 120.0 (CH), 75.5 (CH_2), 34.9 (quat.), 31.5 (CH_2), 30.6 (CH_3), 30.0 (CH_2), 25.4 (CH_2), 22.6 (CH_2), 14.0 (CH_3).

2

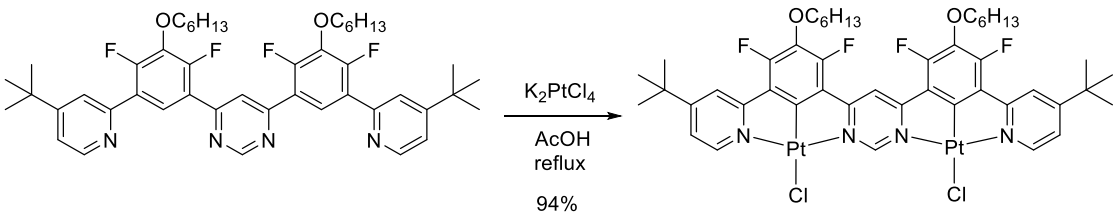

II 2

II (220 mg, 285 μmol, 1 eq.) was dissolved in glacial acetic acid (40 mL) and powdered K_2PtCl_4 (261 mg, 628 μmol, 2.2 eq.) was added to the solution. The reaction mixture was heated to reflux for 24 h under argon atmosphere. After cooling to room temperature, the precipitate was filtered, washed with water and air-dried. The resulting bright red solid (350 mg) was dissolved in DCM (10 mL) and filtered through a microfilter. The solid was precipitated by addition of MeOH (30 mL) to yield the product (330 mg, 94 %) as a bright orange solid.

^{1}H NMR (400 MHz, $CDCl_3$) δ 9.66 (s, 1H), 8.87 (d, *J* = 6.2 Hz, 2H), 8.21 (s, 1H), 7.63 (s, 2H), 7.12 (dd, *J* = 6.1, 2.2 Hz, 2H), 4.18 (t, *J* = 6.5 Hz, 4H), 1.80 – 1.73 (m, 4H), 1.53 – 1.46 (m, 4H), 1.40 – 1.34 (m, 8H), 1.31 (s, 18H), 0.94 (app t, 6H).

^{19}F NMR (376 MHz, $CDCl_3$) δ -119.60 (app d), -119.80 (app d)

Elemental (CHN) analysis: calc. for $C_{46}H_{52}Cl_2F_4N_4O_2Pt_2$, %: C, 44.92; H 4.26; N, 4.56. Found, %: C, 44.62; H, 4.20; N, 4.40.

3

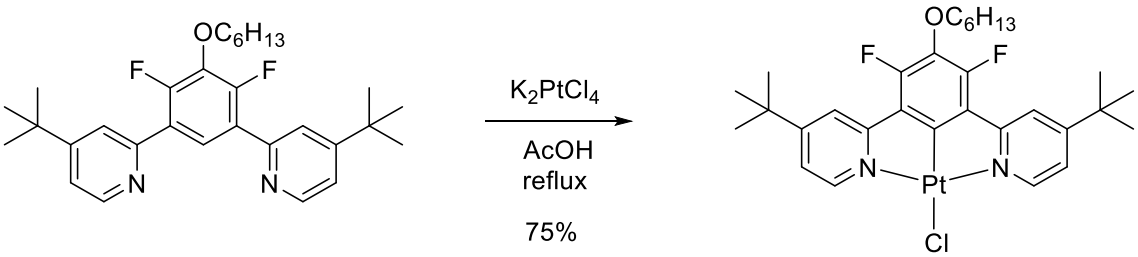

III 3

III (105 mg, 218 μmol, 1 eq.) was dissolved in glacial acetic acid (70 mL) and powdered K_2PtCl_4 (100 mg, 240 μmol, 1.1 eq.) was added to the solution. The reaction mixture was heated to reflux for 24 h under argon atmosphere. About 50 mL of AcOH was removed on a rotary evaporator under reduced pressure; water (50 mL) was added and the precipitate was filtered off and washed with water. After drying in a vacuum oven at 50 ^{0}C for 1 hour, the solid was dissolved in DCM (10 mL) and filtered through a microfilter. The solid was precipitated by addition of MeOH (30 mL) to yield the product (116 mg, 75 %) as an orange-brown solid.

^{1}H NMR (400 MHz, $CDCl_3$) δ 9.14 (d, *J* = 6.2 Hz, 2H), 7.90 (d, *J* = 1.6 Hz, 2H), 7.24 (s, 2H), 4.18 (t, *J* = 6.6 Hz, 2H), 1.82 (app quint, 2H), 1.55 – 1.48 (m, 2H), 1.42 – 1.36 (m, 22H), 0.93 (app t, 3H).

^{19}F NMR (376 MHz, $CDCl_3$) δ -126.66 (t, *J* = 30.1 Hz)

Elemental (CHN) analysis: calc. for $C_{30}H_{37}ClF_2N_2OPt$, %: C, 50.74; H 5.25; N, 3.94. Found, %: C, 50.38; H, 5.19; N, 3.72.

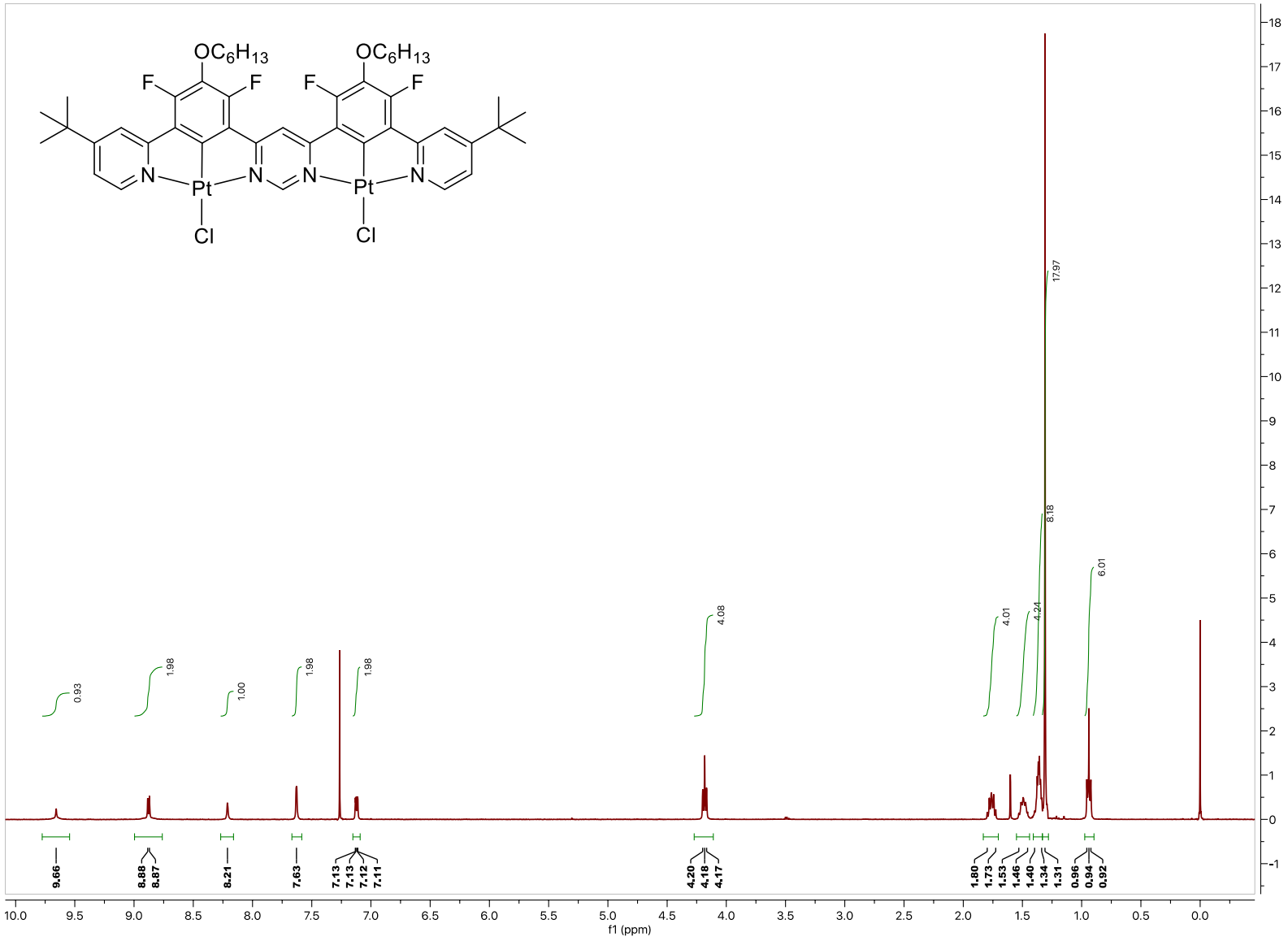
OC6H13
OC6H13
F
F
F
F
N
Pt
N
N
Pt
N
Cl
Cl
0.93
1.98
1.00
1.98
1.98
4.08
4.01
4.24
8.18
17.97
6.01
9.66
8.88
8.87
8.21
7.63
7.13
7.13
7.12
7.11
4.20
4.18
4.17
1.80
1.73
1.53
1.46
1.40
1.34
1.31
0.96
0.94
0.92
f1 (ppm)

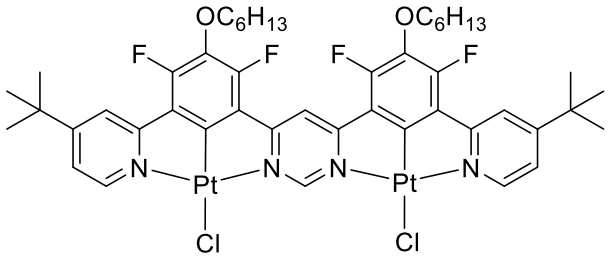
OC6H13
OC6H13
F
F
F
F
N
Pt
N
N
Pt
N
Cl
Cl

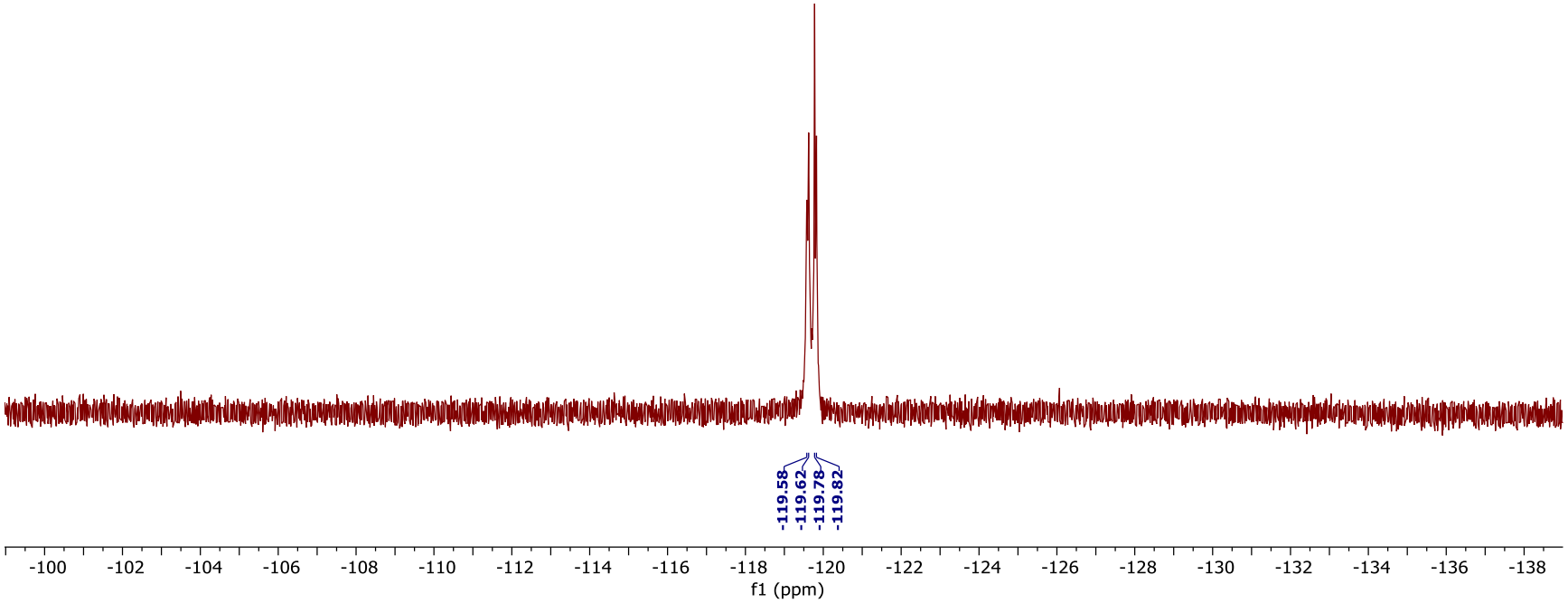
-119.58
-119.62
-119.78
-119.82
-100
-102
-104
-106
-108
-110
-112
-114
-116
-118
-120
-122
-124
-126
-128
-130
-132
-134
-136
-138
f1 (ppm)

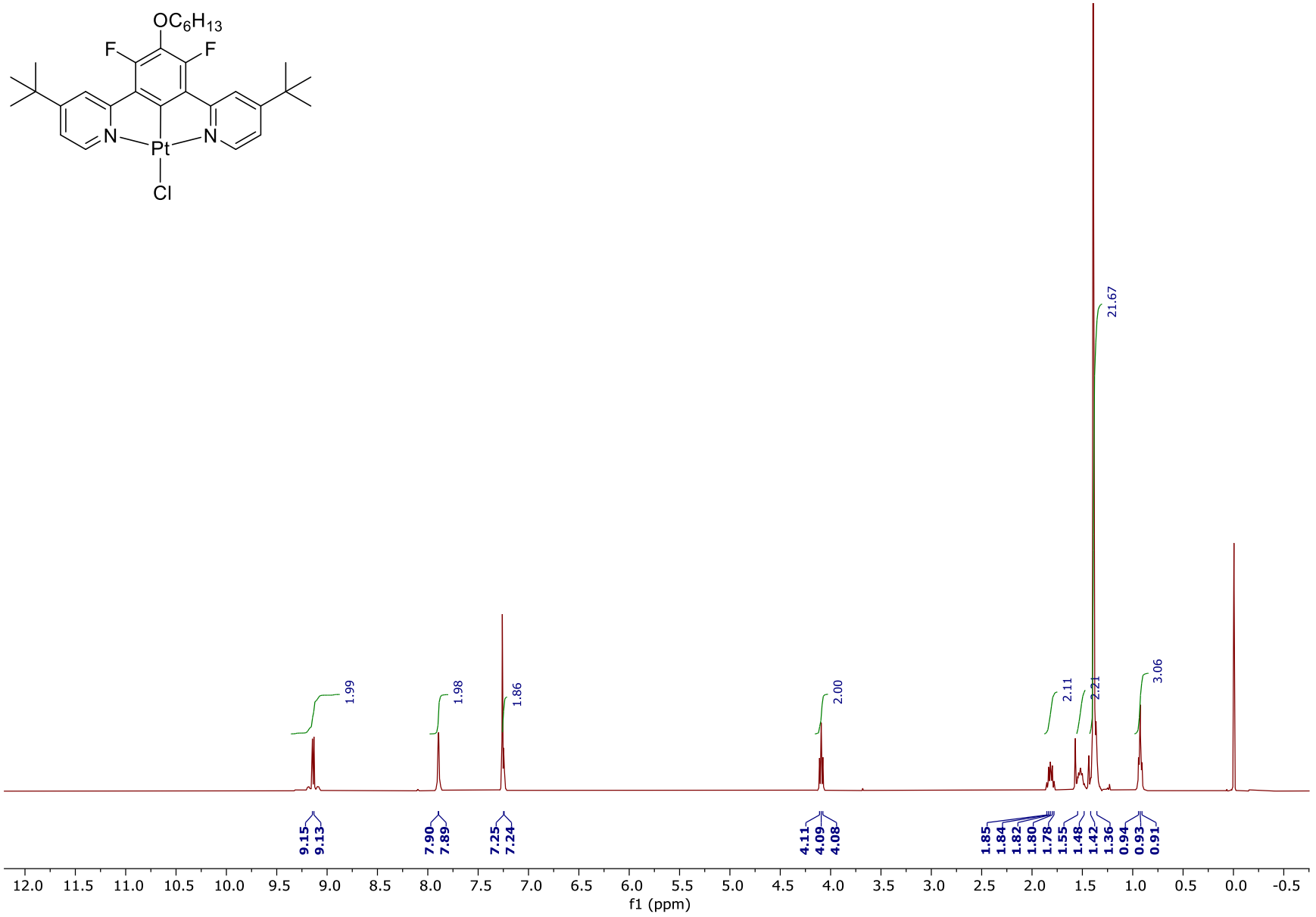
OC6H13
F
F
N
Pt
N
Cl
21.67
1.99
1.98
1.86
2.00
2.11
2.21
3.06
9.15
9.13
7.90
7.89
7.25
7.24
4.11
4.09
4.08
1.85
1.84
1.82
1.80
1.78
1.55
1.48
1.42
1.36
0.94
0.93
0.91
12.0 11.5 11.0 10.5 10.0 9.5 9.0 8.5 8.0 7.5 7.0 6.5 6.0 5.5 5.0 4.5 4.0 3.5 3.0 2.5 2.0 1.5 1.0 0.5 0.0 -0.5
f1 (ppm)

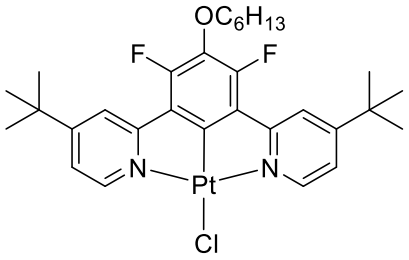
OC6H13
F
F
N
Pt
N
Cl

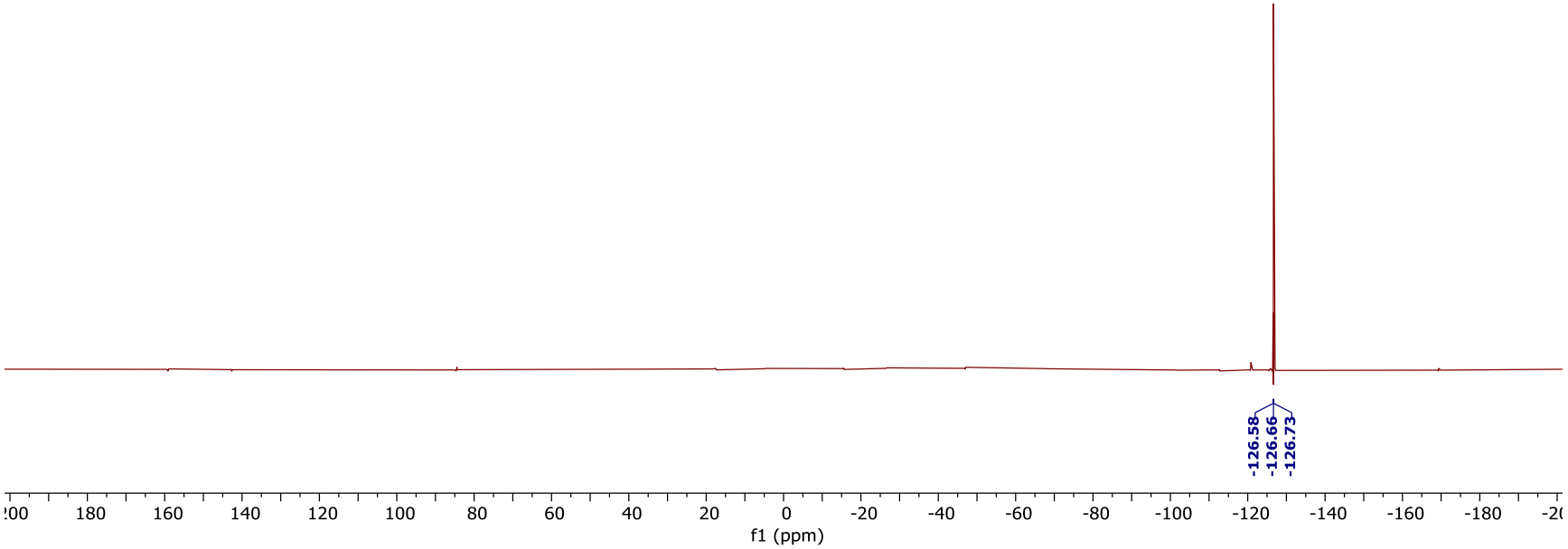
-126.58
-126.66
-126.73
180
160
140
120
100
80
60
40
20
0
-20
-40
-60
-80
-100
-120
-140
-160
-180
f1 (ppm)

3. X-ray crystallography

The X-ray single crystal data for structure **2** were collected using λMoKa radiation (λ = 0.71073 Å) on a Bruker D8Venture (Photon100 CMOS detector, IμS-microsource, focusing mirrors) diffractometer equipped with a Cryostream (Oxford Cryosystems) open-flow nitrogen cryostat at the temperature 120.0(2) K. The structure was solved by intrinsic phasing method and refined by full-matrix least squares on F^2 for all data using Olex2[22] and SHELXTL24[23] software. All non-disordered non-hydrogen atoms were refined anisotropically. Hydrogen atoms were placed in calculated positions and refined using the riding model. Disordered carbon atoms in the structure (C40A and C40B) were refined isotropically with fixed SOF = 0.5. The structure also contains 1/4-occupied disordered DCM solvent molecule. Crystal data and parameters of refinement are listed in the Table S3.1 below. Crystallographic data for the structure have been deposited at CCDC, as supplementary publication CCDC-2088015. These data can be obtained free of charge from The Cambridge Crystallographic Data Centre via www.ccdc.cam.ac.uk/data_request/cif

Table S3.1 Crystal data and structure refinement for complex **2**.

Empirical formula	$C_{46}H_{52}Cl_2F_4N_4O_2Pt_2$ x 0.25 CH_2Cl_2
Formula weight	1251.22
Temperature/K	120.0
Crystal system	triclinic
Space group	P-1
a/Å	10.0468(18)
b/Å	15.698(3)
c/Å	17.546(3)
α/°	64.485(4)
β/°	74.801(5)
γ/°	80.733(5)
Volume/Å^3	2406.4(7)
Z	2
ρ_{calc}g/cm^3	1.727
μ/mm^{-1}	6.001
F(000)	1217.0
Crystal size/mm^3	0.31 × 0.05 × 0.04
Reflections collected	42131
Independent reflections	10494 [R_{int} = 0.1402, R_{sigma} = 0.1611]
Data/restraints/parameters	10494/73/573
Goodness-of-fit on F^2	1.024
Final R indexes [I>=2σ (I)]	R_1 = 0.0805, wR_2 = 0.1817
Final R indexes [all data]	R_1 = 0.1788, wR_2 = 0.2432
Largest diff. peak/hole / e Å^{-3}	6.09/-2.99

4. Theory

a) B3LYP/def2-TZVP/ZORA

Table S4.1 Summary of calculated excited state properties of **2** and **3** in toluene at room temperature.

		2	**3**
TDDFT	**S_1 / eV (nm)**	2.268 (547)	3.013 (412)
	T_1 / eV (nm)	2.006 (618)	2.626 (472)
	ΔE_{ST} / eV	0.262	0.387
	f (S_1)	0.19	6.5×10^{-3}
	k_s^{-1} / s	1.1×10^{-8}	1.8×10^{-7}
SOC-TDDFT	**Γ_1 (triplet) / eV (nm)**	1.929 (643)	2.634 (471)
	Γ_n (singlet) / eV (nm)	2.126 (583) [Γ_7]	*
	ΔE_{ST} / eV	0.197	*
	$\Delta E(\Gamma_3\text{-}\Gamma_1)$, (ZFS) / cm^{-1}	46.4	120.9
	$S_1\text{-}T_1$ SOCME / cm^{-1}	14	1.8
	f (Γ_n) (singlet)	0.13 [Γ_7]	*
	k_s^{-1} / s	1.8×10^{-8}	*
	k_T^{-1} / s	2.2×10^{-4}	9.7×10^{-6}

Note: for explanation of symbols in the table see main article. * Not shown due to low singlet character to the SOC-TDDFT states.

Table S4.2 Summary of relevant TDDFT excited states in **2** (CH_2Cl_2).

Excited state	**Energy / eV**	**Transition**	**Character**
S_1	2.404	HOMO→LUMO (98%)	$d_{xz(Pt1\|Pt2)} + p_{z(Cl1\|Cl2)} + \pi_{ph} \rightarrow \pi_{pyrim}^*$
S_2	2.488	HOMO-1→LUMO (94%)	$d_{xz(Pt1\|Pt2)} + p_{z(Cl1\|Cl2)} + \pi_{ph} \rightarrow \pi_{pyrim}^*$
S_3	2.784	HOMO-3→LUMO (48%) HOMO-2→LUMO (44%)	$d_{xy(Pt1\|Pt2)} + d_{yz(Pt1\|Pt2)} + p_{y(Cl1\|Cl2)} + \pi_{ph} \rightarrow \pi_{pyrim}^*$
T_1	2.115	HOMO→LUMO (94%)	$d_{xz(Pt1\|Pt2)} + p_{z(Cl1\|Cl2)} + \pi_{ph} \rightarrow \pi_{pyrim}^*$
T_2	2.249	HOMO-1→LUMO (87%)	$d_{xz(Pt1\|Pt2)} + p_{z(Cl1\|Cl2)} + \pi_{ph} \rightarrow \pi_{pyrim}^*$
T_3	2.467	HOMO-2→LUMO (77%)	$d_{yz(Pt1\|Pt2)} + \pi_{ph} \rightarrow \pi_{pyrim}^*$

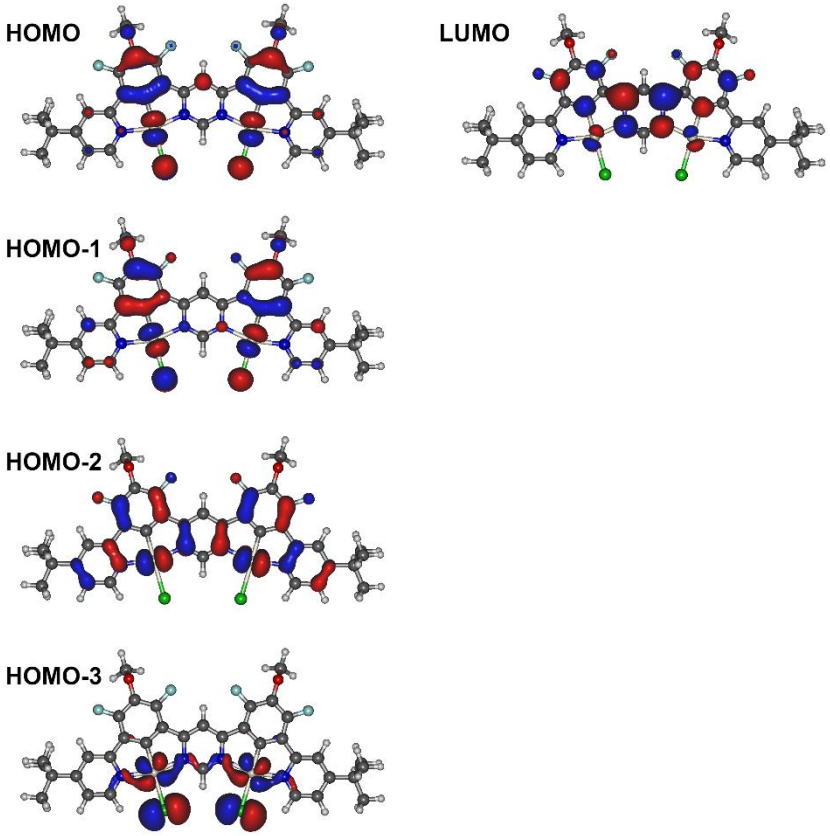

Figure S4.1. Relevant MO iso surfaces of **2**.

Table S4.3 Summary of relevant TDDFT excited states in **3** (CH_2Cl_2).

Excited state	**Energy / eV**	**Transition**	**Character**
S_1	3.142	HOMO→LUMO (97%)	$d_{xz(Pt)} + p_{z(Cl)} + \pi \rightarrow \pi^*$
S_2	3.220	HOMO→LUMO+1 (97%)	$d_{xz(Pt)} + p_{z(Cl)} + \pi \rightarrow \pi^*$
S_3	3.583	HOMO-1→LUMO (97%)	$d_{yz(Pt)} + \pi \rightarrow \pi^*$
T_1	2.679	HOMO→LUMO (63%) HOMO-1→LUMO+1 (21%)	$d_{xz(Pt)} + d_{yz(Pt)} + p_{z(Cl)} + \pi \rightarrow \pi^*$
T_2	2.865	HOMO→LUMO+1 (79%) HOMO-1→LUMO (13%)	$d_{xz(Pt)} + d_{yz(Pt)} + p_{z(Cl)} + \pi \rightarrow \pi^*$
T_3	3.064	HOMO-1→LUMO+1 (53%) HOMO→LUMO (31%)	$d_{xz(Pt)} + d_{yz(Pt)} + p_{z(Cl)} + \pi \rightarrow \pi^*$

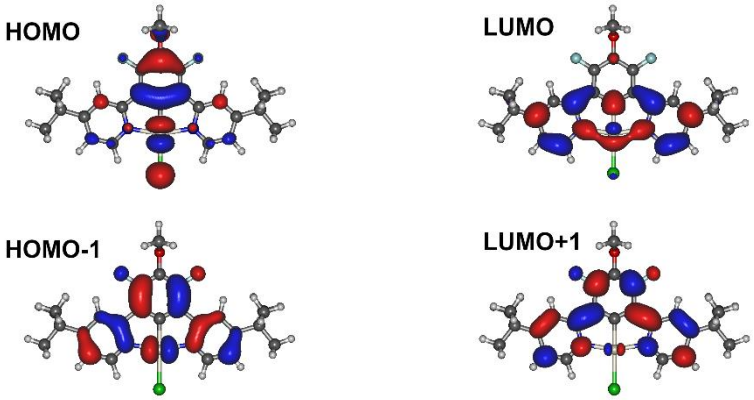

Figure S4.2. Relevant MO isosurfaces of **3**.

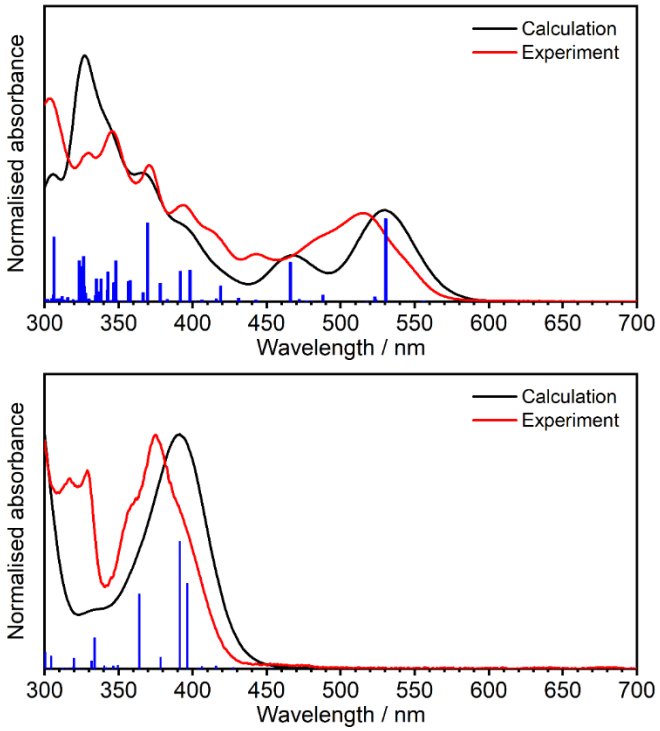

Figure S4.3. Simulated and experimental absorption spectra of **2** (top) and **3** (bottom) in CH_2Cl_2.

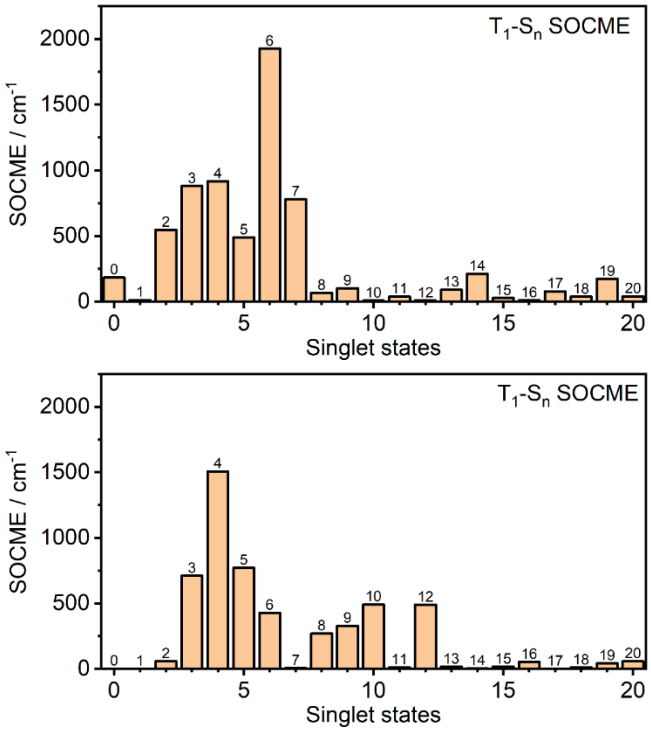

Figure S4.4. SOCME (spin-orbit coupling matrix element) for T_1-S_n pairs for **2** (top) and **3** (bottom) in CH_2Cl_2. Note the numbers above bars indicate number of the singlet S_n excited state, where 0 indicates ground state S_0.

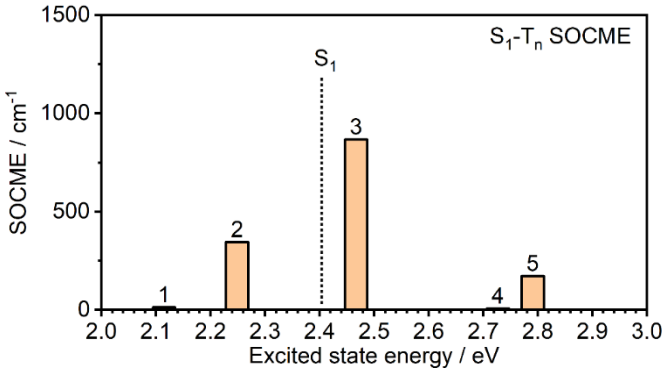

Figure S4.5. SOCME between S_1 and T_n states in **2** (CH_2Cl_2). Note the numbers above bars indicate number of the T_n excited state.

Table S4.4 Composition of relevant SOC states of **2** and **3** in CH_2Cl_2.

Complex	State	Energy / eV	Contribution of zero-order states*
2	Γ_1	2.1021	$T_1^{Ms=1}$ (43.1%), $T_1^{Ms=-1}$ (43.1%), S_6 (5.3%)
	Γ_2	2.1068	$T_1^{Ms=0}$ (57.3%), $T_1^{Ms=1}$ (15.0%), $T_1^{Ms=-1}$ (15.0%)
	Γ_3	2.1074	$T_1^{Ms=0}$ (29.8%), $T_1^{Ms=1}$ (28.7%), $T_1^{Ms=-1}$ (28.7%)
	Γ_7	2.3381	S_1 (69.4%), $T_3^{Ms=0}$ (12.3%)
3	Γ_1	2.7274	$T_1^{Ms=0}$ (82.2%), $T_5^{Ms=1}$ (5.3%), $T_5^{Ms=-1}$ (5.3%)
	Γ_2	2.7280	$T_1^{Ms=1}$ (41.3%), $T_1^{Ms=-1}$ (41.3%), $T_5^{Ms=0}$ (10.2%)
	Γ_3	2.7373	$T_1^{Ms=1}$ (43.8%), $T_1^{Ms=-1}$ (43.8%), S_4 (5.9%)
	Γ_7	2.9816	S_1 (20.1%), $T_4^{Ms=0}$ (18.1%), $T_7^{Ms=1}$ (23.3%), $T_7^{Ms=-1}$ (23.3%)

* States with contributions < 5% are not shown.

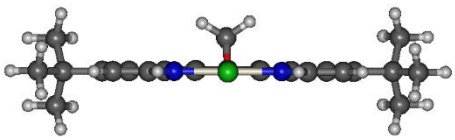

Figure S4.6. Side view of **3**. Note the Pt(*N^C^N*) unit remains flat.

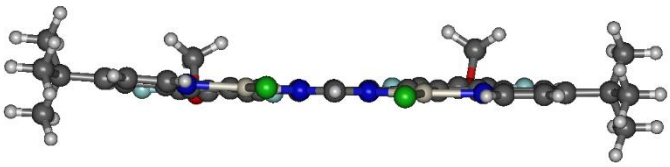

Figure S4.7. Side view of **2**. Note the di-Pt(*N^C^N*) unit is slightly distorted.

b) B3LYP/def2-SVP

Overall, the results obtained with the smaller def2-SVP basis set are very similar to those obtained using the larger def2-TZVP basis. This is especially true for ground state calculations. However, using the former basis set it is not possible to account for relativistic effects as the ZORA-corrected basis sets for def2-SVP cannot be applied for 3rd row transition metals, such as platinum.

Interestingly, there is a great similarity between the S_0 and T_1 geometry in **3** which is not surprising given its very rigid structure (**Figure S4.12** and **Figure S4.13**). On the other hand, the T_1 geometry of **2** is more planar than the respective S_0 structure (**Figure S4.14** and **Figure S4.15**). Even though the geometry of complex **2** is slightly different in the excited state in respect to the ground state, the respective character of lowest excited states remains virtually the same, leading to the same conclusion about the RISC/ISC process involving S_1 and T_2 / T_3 states, as stated in the main article (compare **Table S4.2**, **Table S4.5**, and **Table S4.6**).

Table S4.5 Summary of the lowest TDDFT excited states in **2** (CH_2Cl_2) at S_0 geometry.

Excited state	**Energy / eV**	**Transition**	**Character**
S_1	2.389	HOMO→LUMO (96%)	$d_{xz(Pt1\|Pt2)} + p_{z(Cl1\|Cl2)} + \pi_{ph} \rightarrow \pi_{pyrim}^*$
S_2	2.479	HOMO-1→LUMO (94%)	$d_{xz(Pt1\|Pt2)} + p_{z(Cl1\|Cl2)} + \pi_{ph} \rightarrow \pi_{pyrim}^*$
S_3	2.487	HOMO-2→LUMO (97%)	$d_{xy(Pt1\|Pt2)} + p_{y(Cl1\|Cl2)} + \pi_{ph} \rightarrow \pi_{pyrim}^*$
T_1	2.023	HOMO→LUMO (95%)	$d_{xz(Pt1\|Pt2)} + p_{z(Cl1\|Cl2)} + \pi_{ph} \rightarrow \pi_{pyrim}^*$
T_2	2.136	HOMO-1→LUMO (94%)	$d_{xz(Pt1\|Pt2)} + p_{z(Cl1\|Cl2)} + \pi_{ph} \rightarrow \pi_{pyrim}^*$
T_3	2.535	HOMO-3→LUMO (83%)	$d_{yz(Pt1\|Pt2)} + \pi_{ph} \rightarrow \pi_{pyrim}^*$

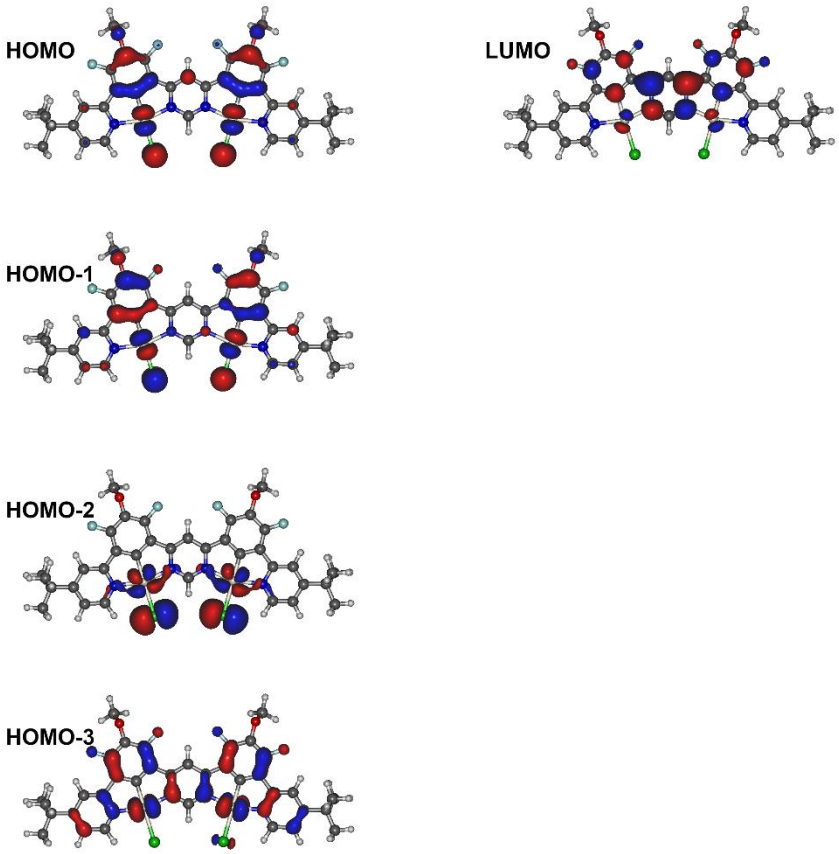

Figure S4.8. Relevant MO isosurfaces of **2** at S_0 geometry.

Table S4.6 Summary of the lowest TDDFT excited states in **2** (CH_2Cl_2) at T_1 geometry.

Excited state	**Energy / eV**	**Transition**	**Character**
S_1	2.230	HOMO→LUMO (96%)	$d_{xz(Pt1\|Pt2)} + p_{z(Cl1\|Cl2)} + \pi_{ph} \rightarrow \pi_{pyrim}^*$
S_2	2.323	HOMO-1→LUMO (94%)	$d_{xz(Pt1\|Pt2)} + p_{z(Cl1\|Cl2)} + \pi_{ph} \rightarrow \pi_{pyrim}^*$
S_3	2.368	HOMO-2→LUMO (97%)	$d_{xy(Pt1\|Pt2)} + p_{y(Cl1\|Cl2)} + \pi_{ph} \rightarrow \pi_{pyrim}^*$
T_1	1.835	HOMO→LUMO (96%)	$d_{xz(Pt1\|Pt2)} + p_{z(Cl1\|Cl2)} + \pi_{ph} \rightarrow \pi_{pyrim}^*$
T_2	1.959	HOMO-1→LUMO (95%)	$d_{xz(Pt1\|Pt2)} + p_{z(Cl1\|Cl2)} + \pi_{ph} \rightarrow \pi_{pyrim}^*$
T_3	2.357	HOMO-3→LUMO (89%)	$d_{yz(Pt1\|Pt2)} + \pi_{ph} \rightarrow \pi_{pyrim}^*$

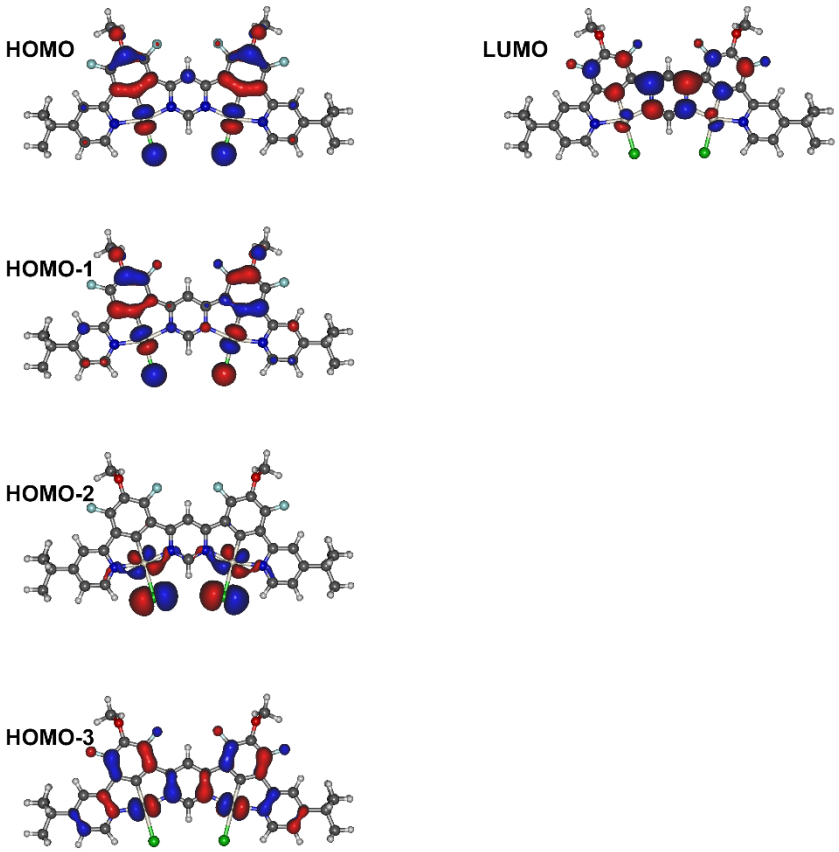

Figure S4.9. Relevant MO isosurfaces of **2** at T_1 geometry.

Table S4.7 Summary of the lowest TDDFT excited states in **3** (CH_2Cl_2) at S_0 geometry.

Excited state	**Energy / eV**	**Transition**	**Character**
S_1	3.195	HOMO→LUMO (95%)	$d_{xz(Pt)} + p_{z(Cl)} + \pi \rightarrow \pi^*$
S_2	3.195	HOMO→LUMO+1 (93%)	$d_{xz(Pt)} + p_{z(Cl)} + \pi \rightarrow \pi^*$
S_3	3.686	HOMO-1→LUMO (94%)	$d_{yz(Pt)} + \pi \rightarrow \pi^*$
T_1	2.763	HOMO→LUMO (80%) HOMO-1→LUMO+1 (11%)	$d_{xz(Pt)} + d_{yz(Pt)} + p_{z(Cl)} + \pi \rightarrow \pi^*$
T_2	2.820	HOMO→LUMO+1 (90%)	$d_{xz(Pt)} + p_{z(Cl)} + \pi \rightarrow \pi^*$
T_3	3.176	HOMO-1→LUMO+1 (71%) HOMO→LUMO (15%)	$d_{xz(Pt)} + d_{yz(Pt)} + p_{z(Cl)} + \pi \rightarrow \pi^*$

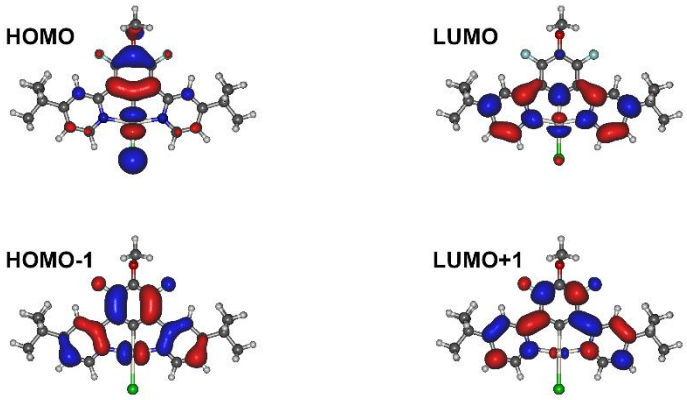

Figure S4.10. Relevant MO isosurfaces of **3** at S_0 geometry.

Table S4.8 Summary of the lowest TDDFT excited states in **3** (CH_2Cl_2) at T_1 geometry.

Excited state	**Energy / eV**	**Transition**	**Character**
S_1	2.694	HOMO→LUMO (93%)	$d_{xz(Pt)} + p_{z(Cl)} + \pi \rightarrow \pi^*$
S_2	2.848	HOMO→LUMO+1 (94%)	$d_{xz(Pt)} + p_{z(Cl)} + \pi \rightarrow \pi^*$
S_3	3.092	HOMO-2→LUMO (91%)	$d_{xy(Pt)} + p_{y(Cl)} + \pi \rightarrow \pi^*$
T_1	2.125	HOMO→LUMO (93%)	$d_{xz(Pt)} + p_{z(Cl)} + \pi \rightarrow \pi^*$
T_2	2.380	HOMO→LUMO+1 (96%)	$d_{xz(Pt)} + p_{z(Cl)} + \pi \rightarrow \pi^*$
T_3	2.951	HOMO-1→LUMO (78%)	$d_{yz(Pt)} + \pi \rightarrow \pi^*$

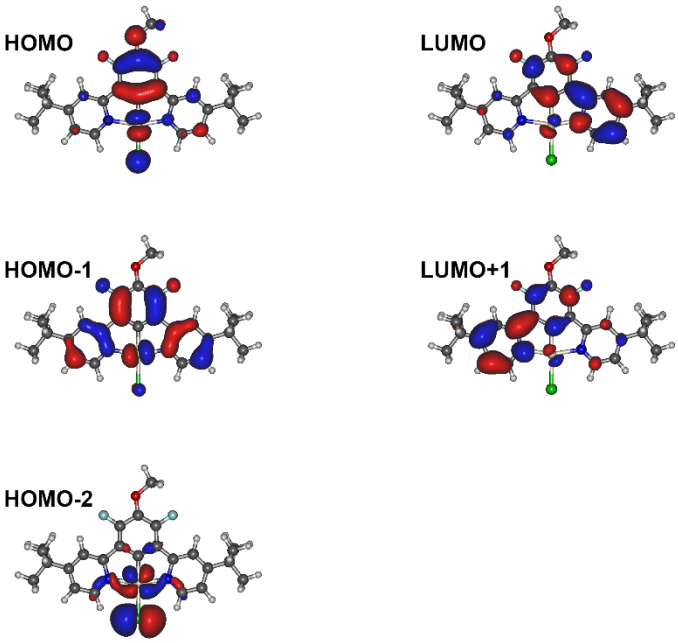

Figure S4.11. Relevant MO isosurfaces of **3** at T_1 geometry.

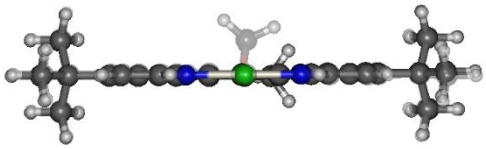

Figure S4.12. Superimposed S_0 (lighter hue) and T_1 (darker hue) geometries of **3** in side view.

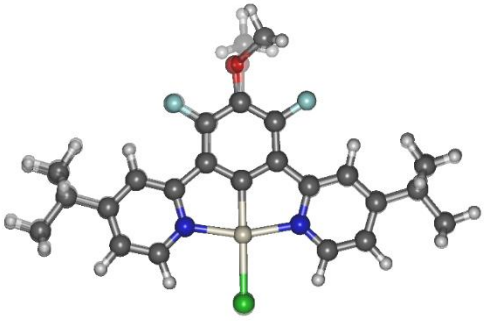

Figure S4.13. Superimposed S_0 (lighter hue) and T_1 (darker hue) geometries of **3** in top view.

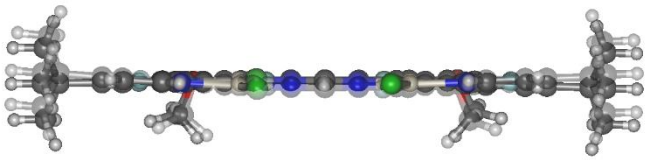

Figure S4.14. Superimposed S_0 (lighter hue) and T_1 (darker hue) geometries of **2** in side view.

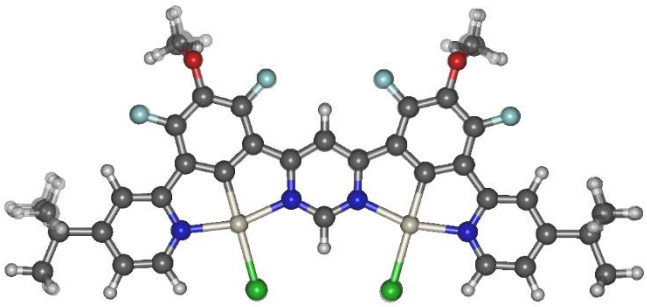

Figure S4.15. Superimposed S_0 (lighter hue) and T_1 (darker hue) geometries of **2** in top view.

5. Photophysics

c) Solution state

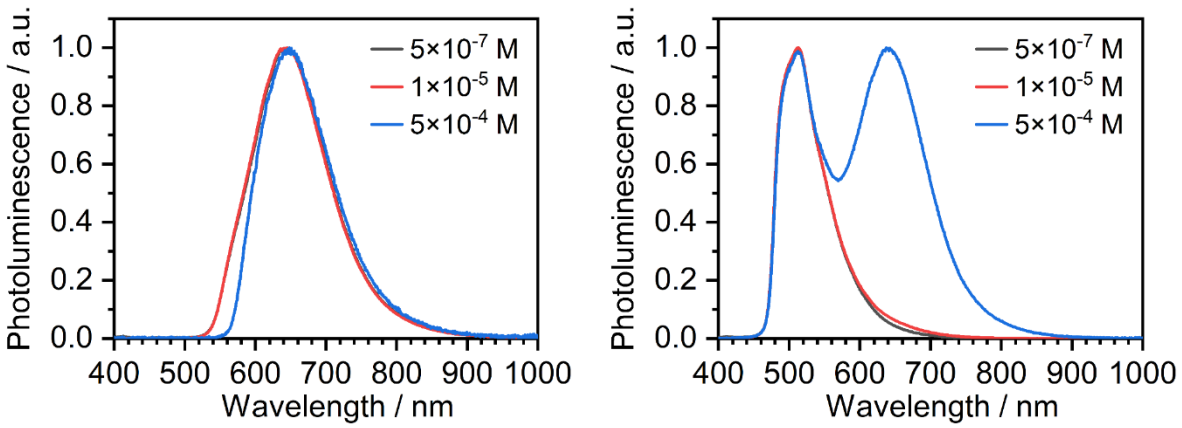

Figure S5.1. Normalised photoluminescence spectra of **2** (left) and **3** (right) in degassed DCM at various concentrations indicated in figure legend.

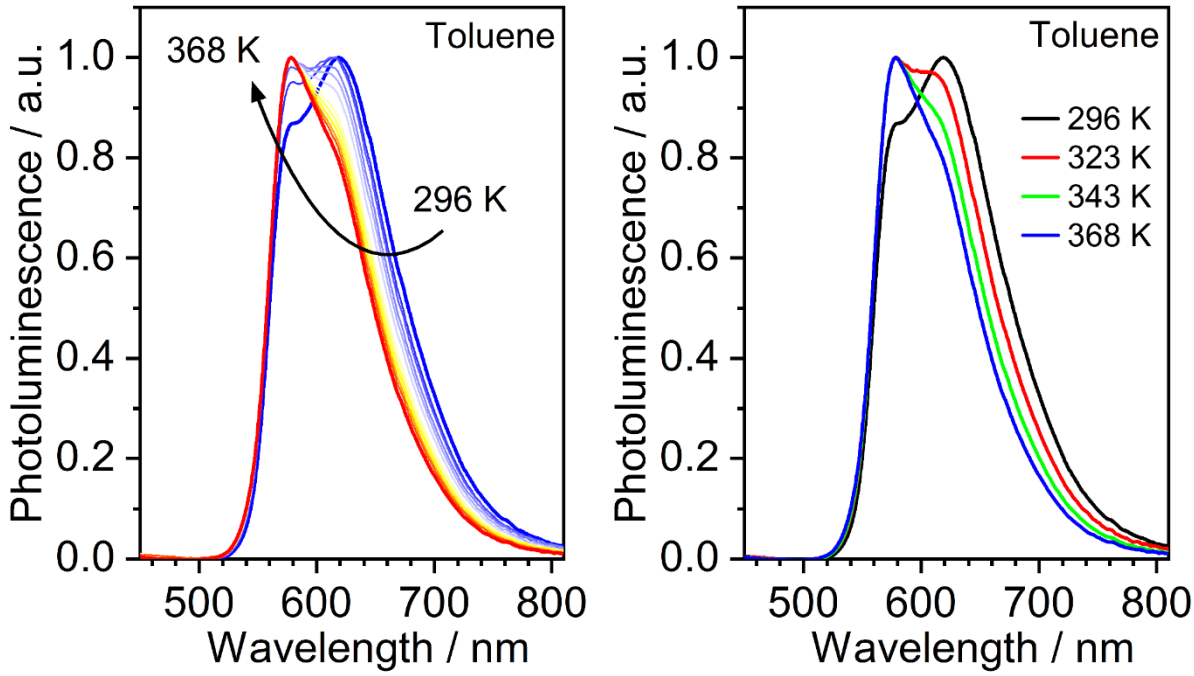

Figure S5.2. Normalised photoluminescence spectra of **2** in deoxygenated toluene at various temperatures indicated in figure legend, c ≈ 10^{-5} M.

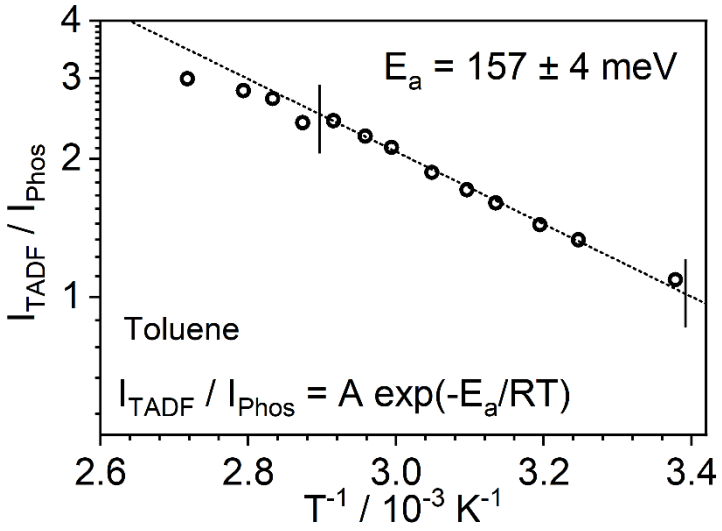

Figure S5.3. TADF-to-phosphorescence ratio in function of temperature in deoxygenated toluene. Note the short vertical lines indicate the experimental data points used for fitting.

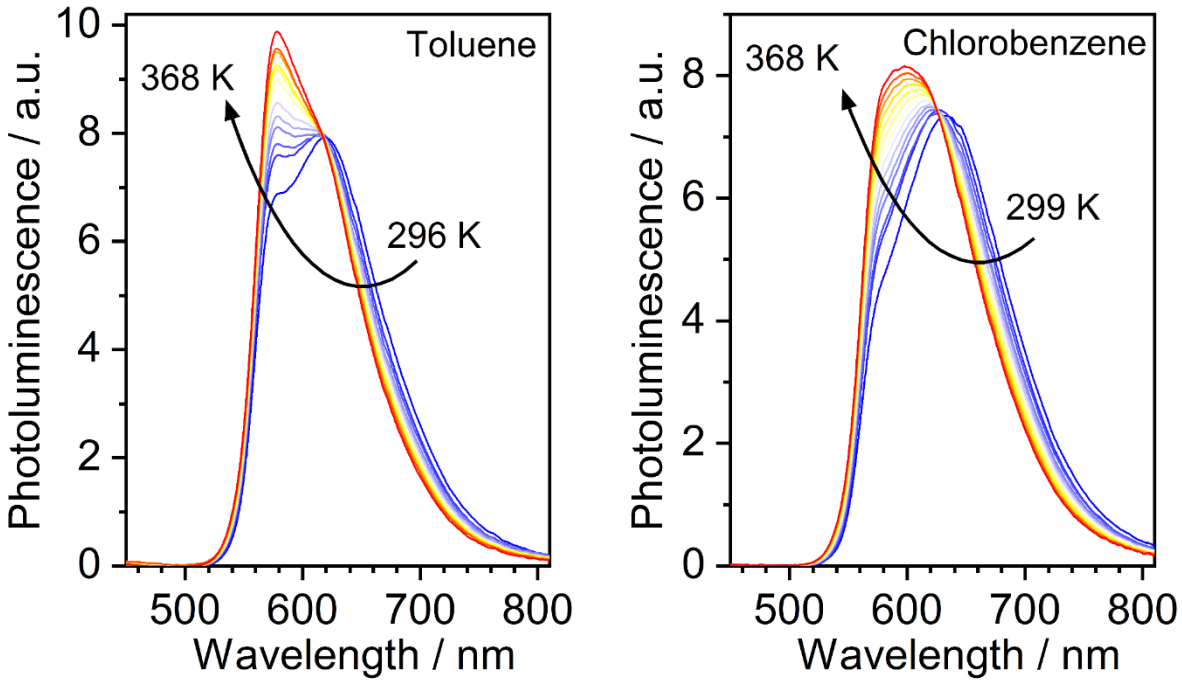

Figure S5.4. Area normalised photoluminescence spectra of **2** in deoxygenated solvents: toluene (left) and chlorobenzene (right) at various temperatures indicated in figure legend, c ≈ 10^{-5} M. Note iso-emissive points are clearly visible in both cases.

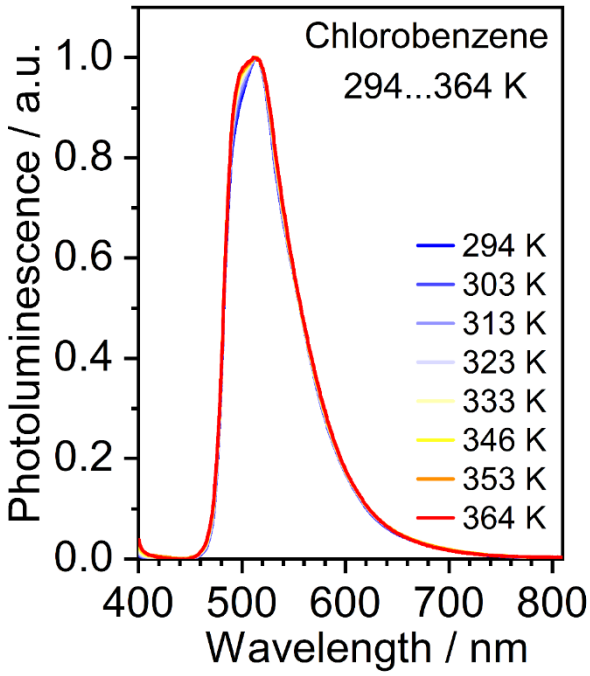

Figure S5.5. Normalised photoluminescence spectra of **3** in chlorobenzene at various temperatures indicated in figure legend, $c \approx 10^{-5}$ M.

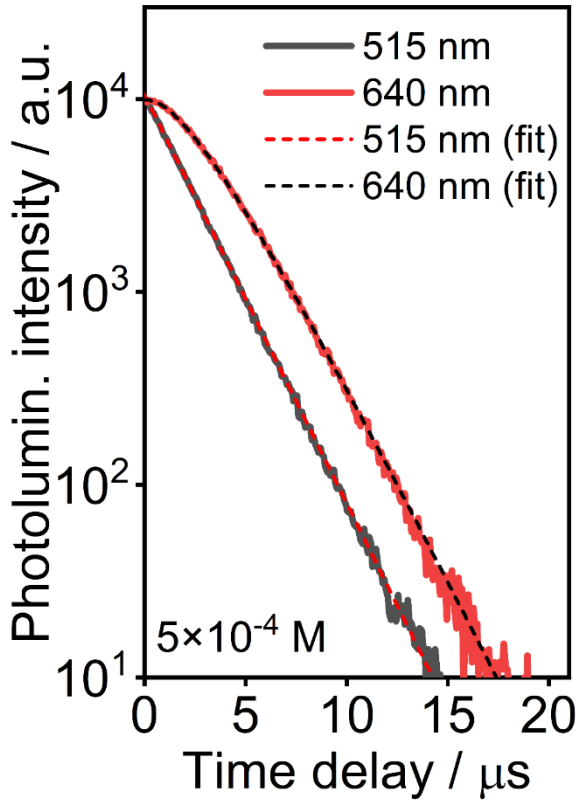

Figure S5.6. Photoluminescence decay of **3** at 5×10^{-5} M concentration in degassed DCM. The dark gray line (515 nm) represents exciton, "monomer" decay, while the red line (640 nm) represents excimer decay. Exciton decay is fitted with monoexponential expression 1, while excimer with biexponential expression 2. The respective lifetime values for exciton and excimer decay are: τ_M = 2.0 μs and τ_E = 1.7 μs, respectively.

$$I(t) = A \cdot exp\left(-\frac{t}{\tau_M}\right) \quad \textbf{(1)}$$

$$I(t) = A\left[exp\left(-\frac{t-t_0}{\tau_M}\right) - exp\left(-\frac{t-t_0}{\tau_E}\right)\right] \quad \textbf{(2)}$$

The equations 1 and 2 are used for fitting of monoexponential exciton ("monomer") decay (1) and biexponential excimer decay (2), where: *I(t)* – luminescence intensity, a.u.; *A* – pre-exponential factor, a.u.; *t* – time, s; t_0 – correction for decay not starting from t = 0, s; τ_M – exciton ("monomer") decay constant at given conditions, s; τ_E – excimer decay constant, s.

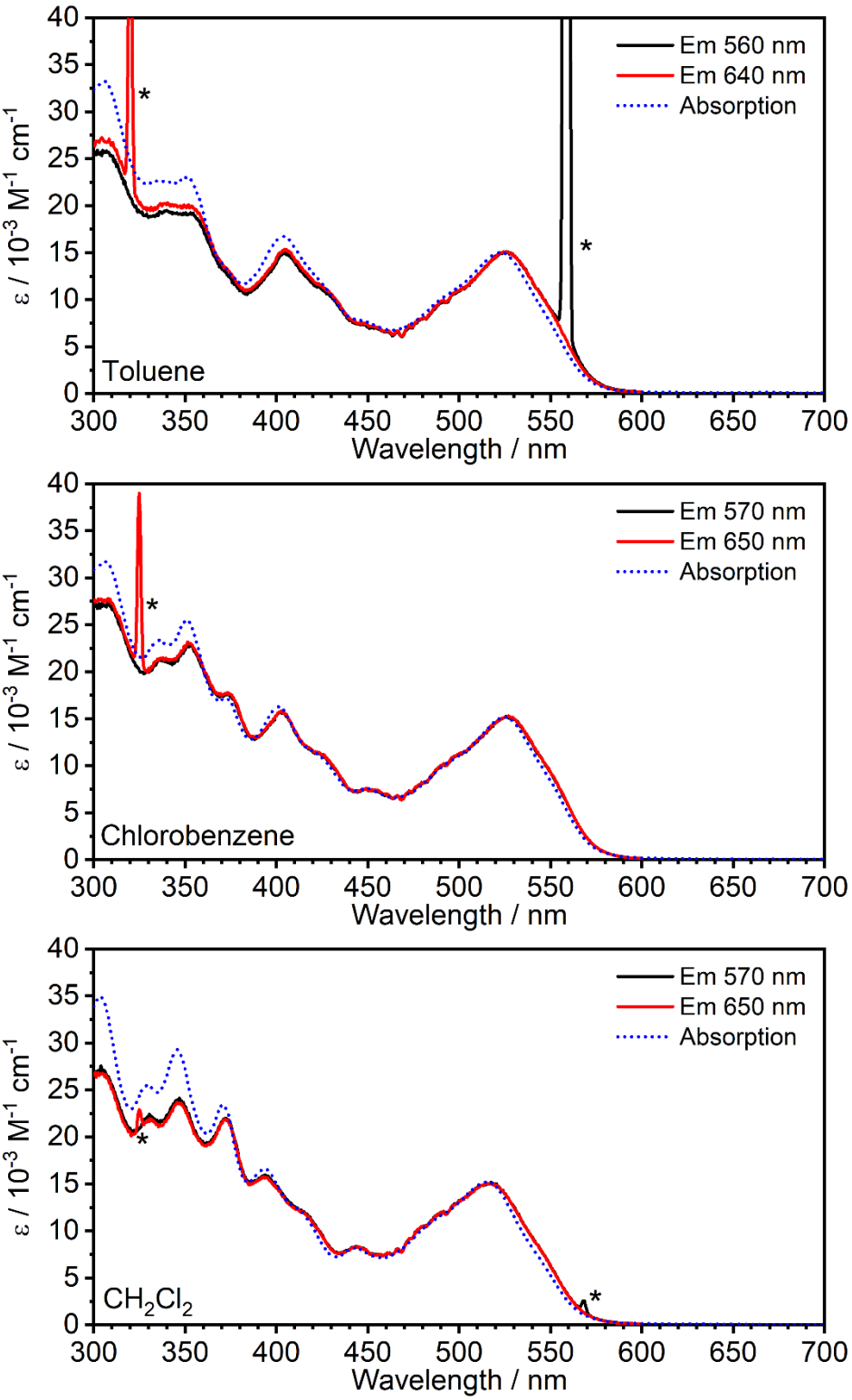

Figure S5.7. Absorption and excitation spectra of **2** in solvents indicated in each figure, c = 10^{-5} M.

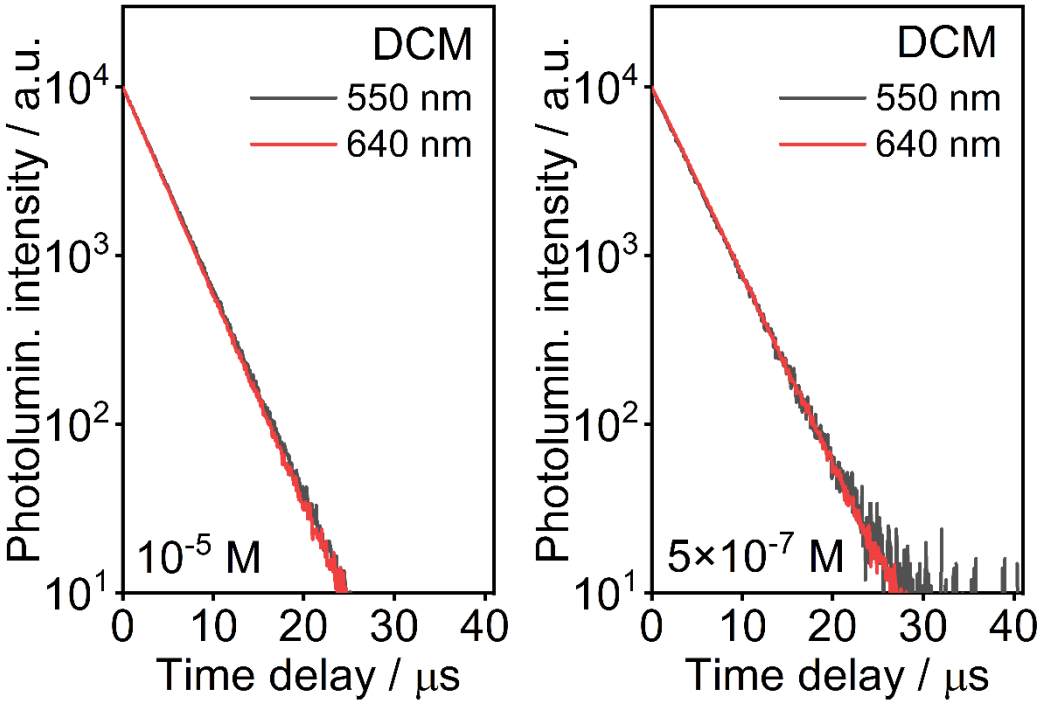

Figure S5.8. Photoluminescence decay traces of **2** in DCM recorded at the two wavelengths attributed to TADF (550 nm) and phosphorescence (640 nm). Note the two bands have identical decay characteristics.

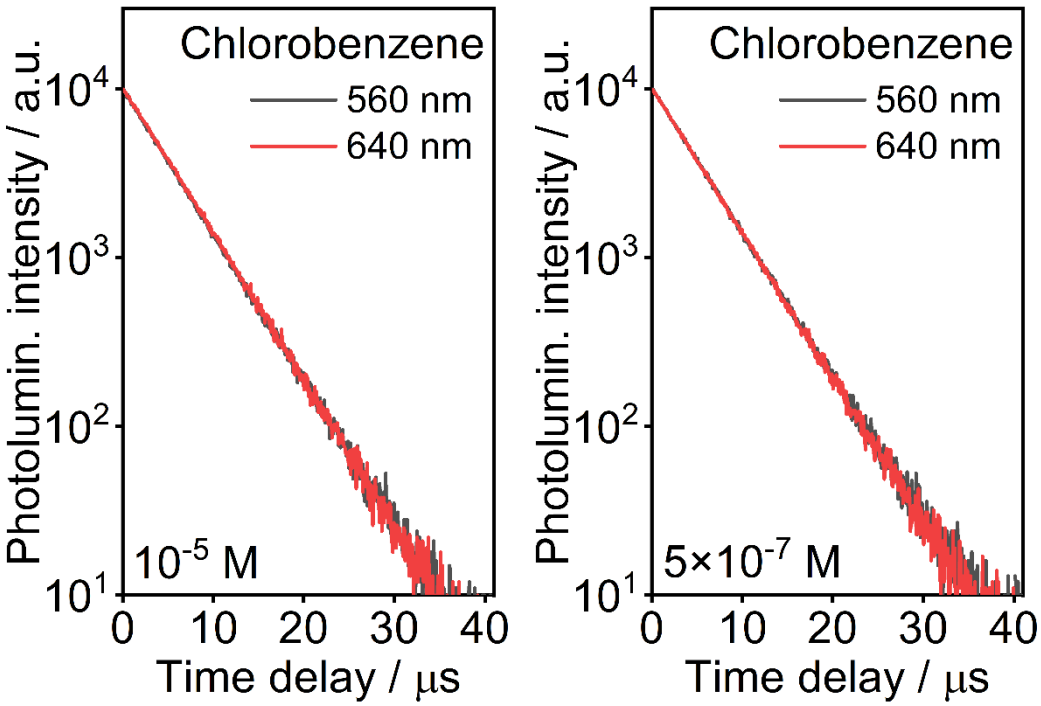

Figure S5.9. Photoluminescence decay traces of **2** in chlorobenzene recorded at the two wavelengths attributed to TADF (560 nm) and phosphorescence (640 nm). Note the two bands have identical decay characteristics.

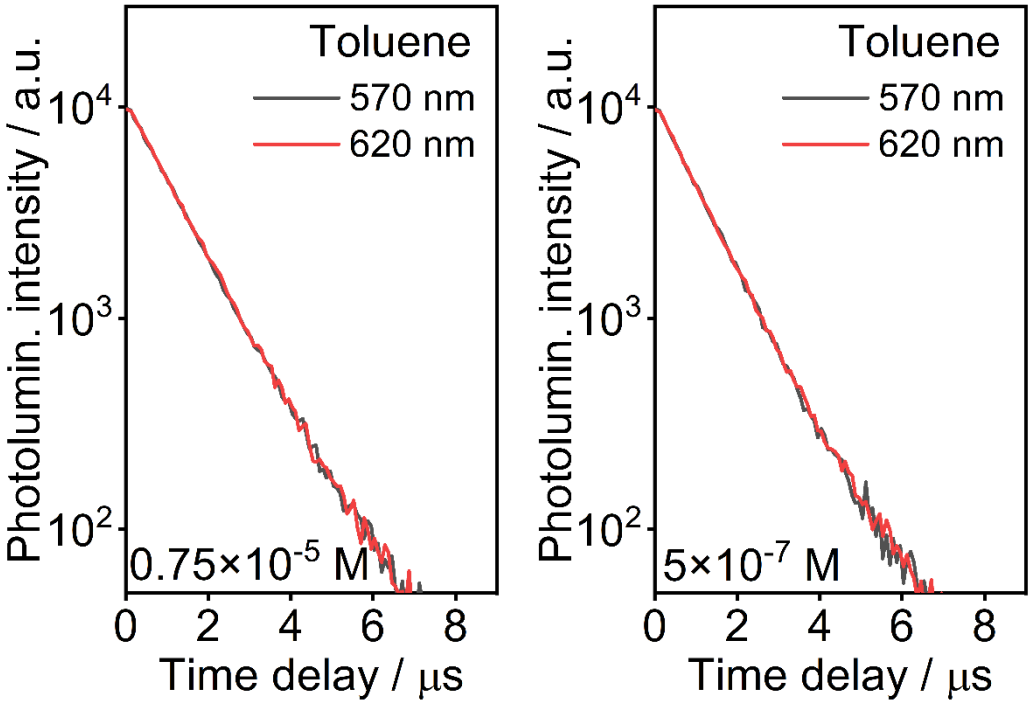

Figure S5.10. Photoluminescence decay traces of **2** in toluene recorded at the two wavelengths attributed to TADF (570 nm) and phosphorescence (620 nm). Note the two bands have identical decay characteristics.

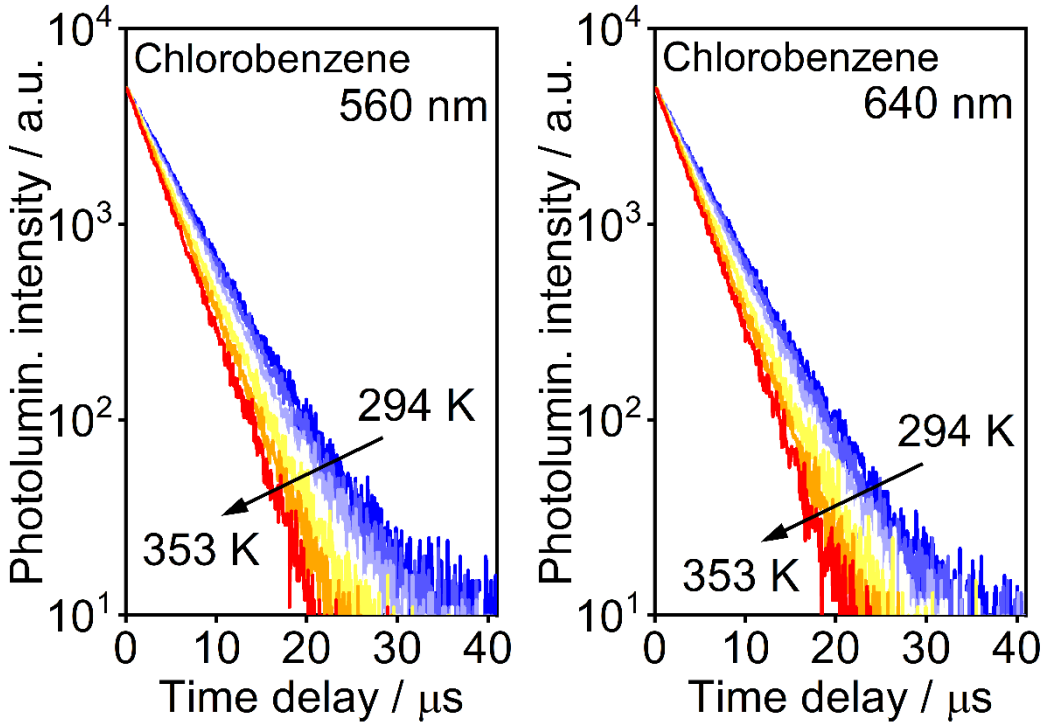

Figure S5.11. Photoluminescence decay traces of **2** (c = 10^{-5} M) at various temperatures in chlorobenzene recorded at the two wavelengths attributed to TADF (560 nm) and phosphorescence (640 nm). Note the two bands have identical decay characteristics.

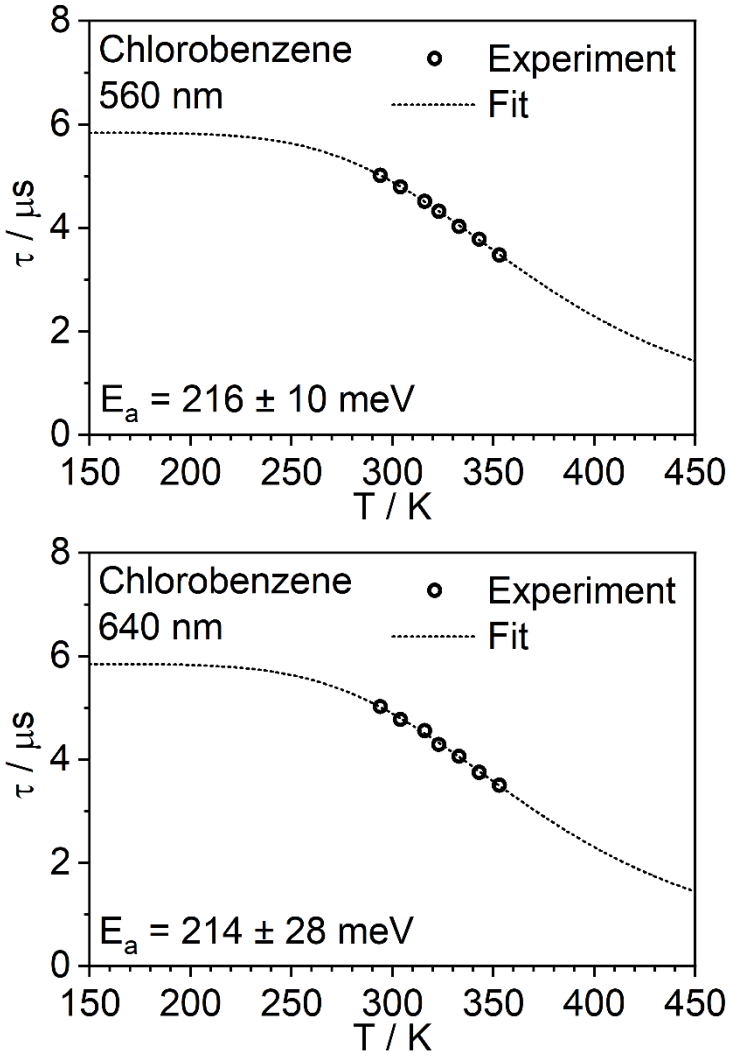

Figure S5.12. Photoluminescence lifetime of **2** (c = 10^{-5} M) at various temperatures in chlorobenzene recorded at the two wavelengths attributed to TADF (560 nm) and phosphorescence (640 nm). Note the two bands have identical decay characteristics and both give same E_a from the fit (eq. 1 in main article). The E_a values obtained are identical to the figure obtained from the steady state spectra in Figure 5b.

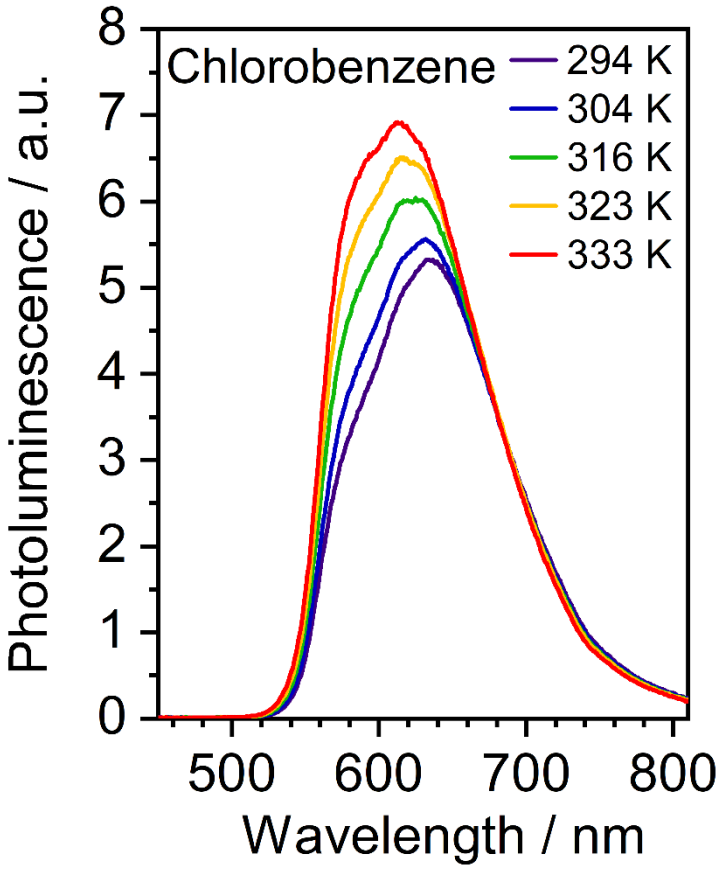

Figure S5.13. Photoluminescence lifetime of **2** at various temperatures in chlorobenzene recorded at the two wavelengths attributed to TADF (560 nm) and phosphorescence (640 nm). Note the two bands have identical decay characteristics and both give same E_a from the fit (eq. 1 in main article). The E_a values obtained are identical to the figure obtained from the steady state spectra in Figure 5b. Note the iso-emissive point at 685 nm.

d) Solid film (polymer matrix)

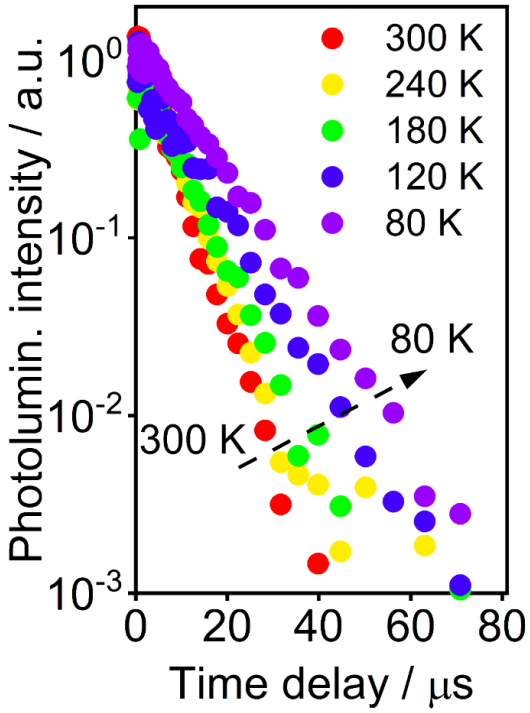

Figure S5.14. Photoluminescence decay traces of **2** in polystyrene film (0.1 % w/w) at temperatures from 300 to 80 K.

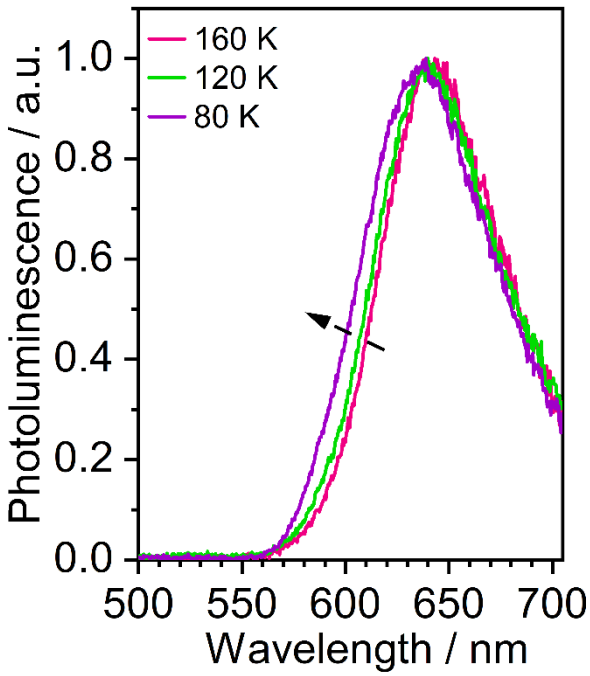

Figure S5.15. Photoluminescence spectra of **2** in polystyrene film (0.1 % w/w) at temperatures from 160 to 80 K.

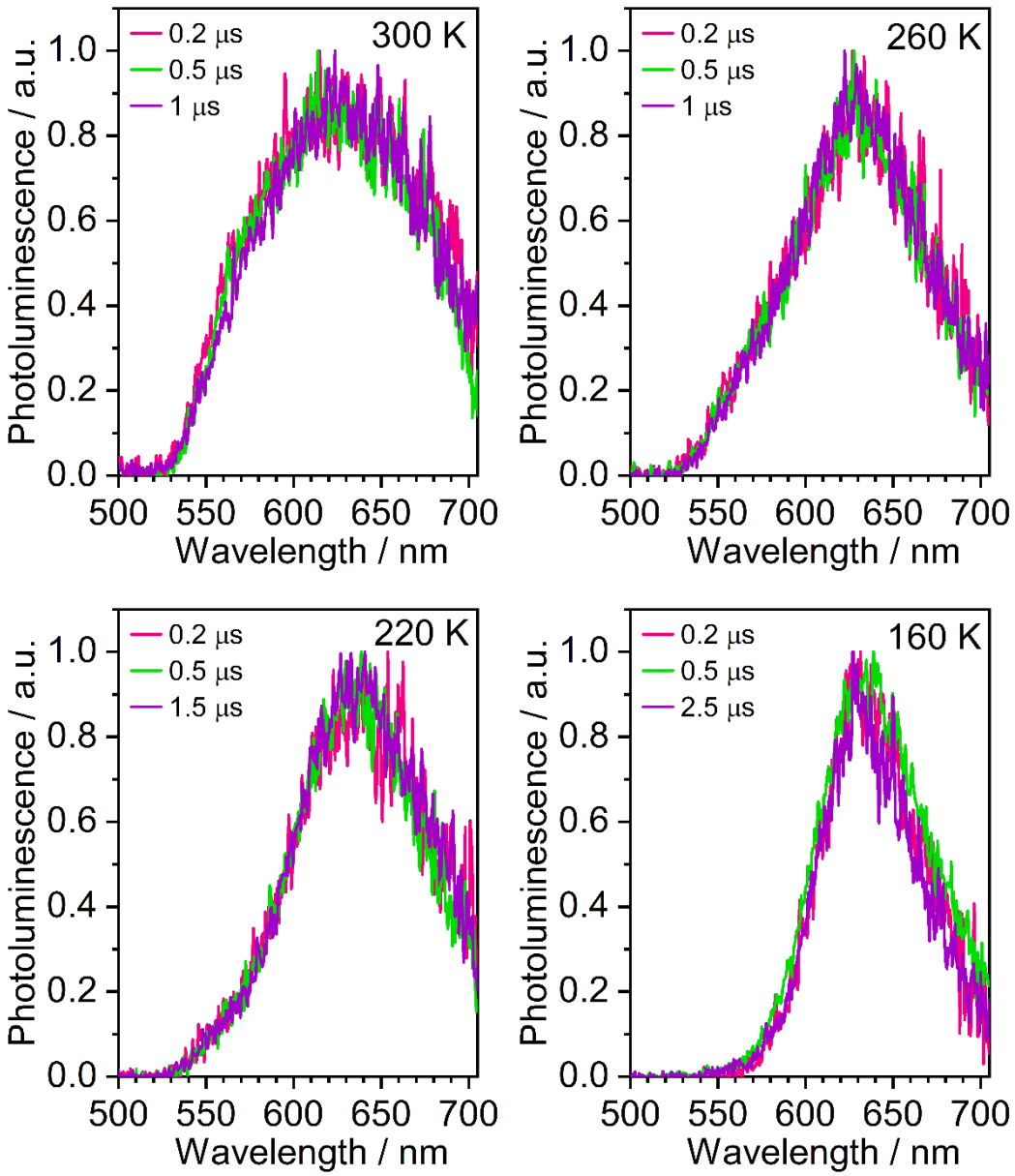

Figure S5.16. Time-resolved photoluminescence spectra of **2** in polystyrene film (0.1 % w/w).

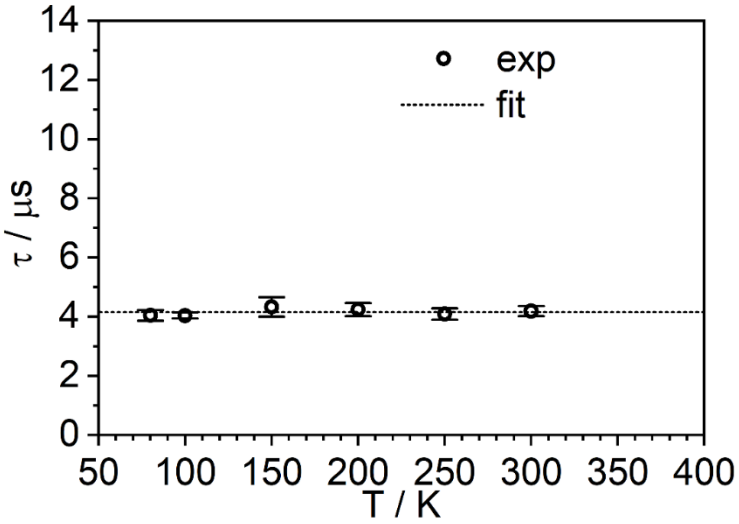

Figure S5.17. Photoluminescence decay lifetime of **3** in polystyrene film (0.1 % w/w) at temperatures from 300 to 80 K. Fit represents a horizontal line, $\tau = 4.2$ μs.

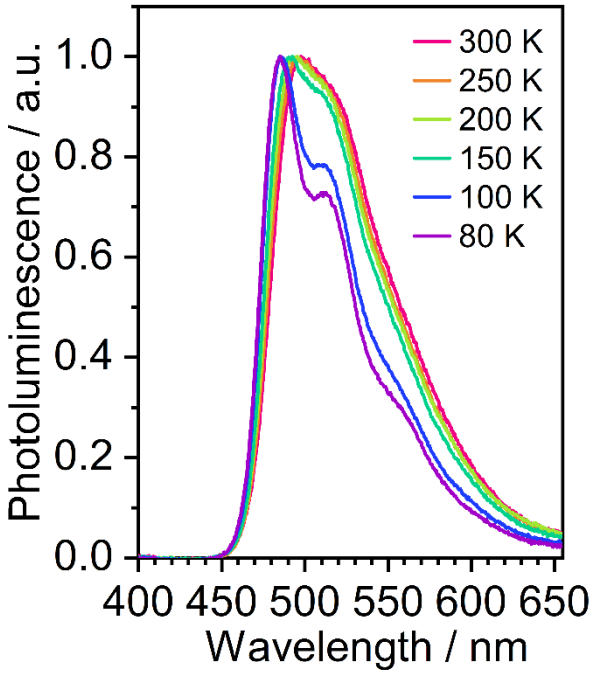

Figure S5.18. Photoluminescence spectra of **3** in polystyrene film (0.1 % w/w) at temperatures from 300 to 80 K.

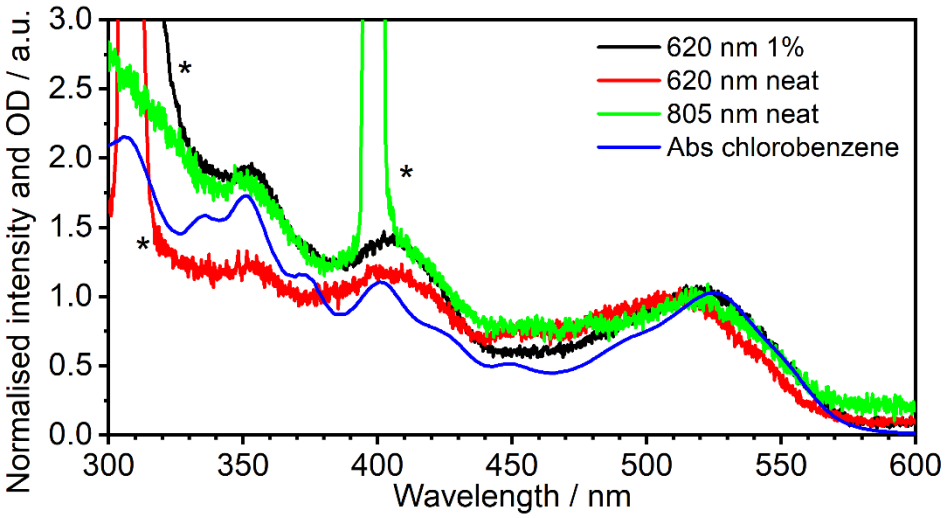

Figure S5.19. Absorption spectrum in chlorobenzene and excitation spectra of **2** in polystyrene and neat film.

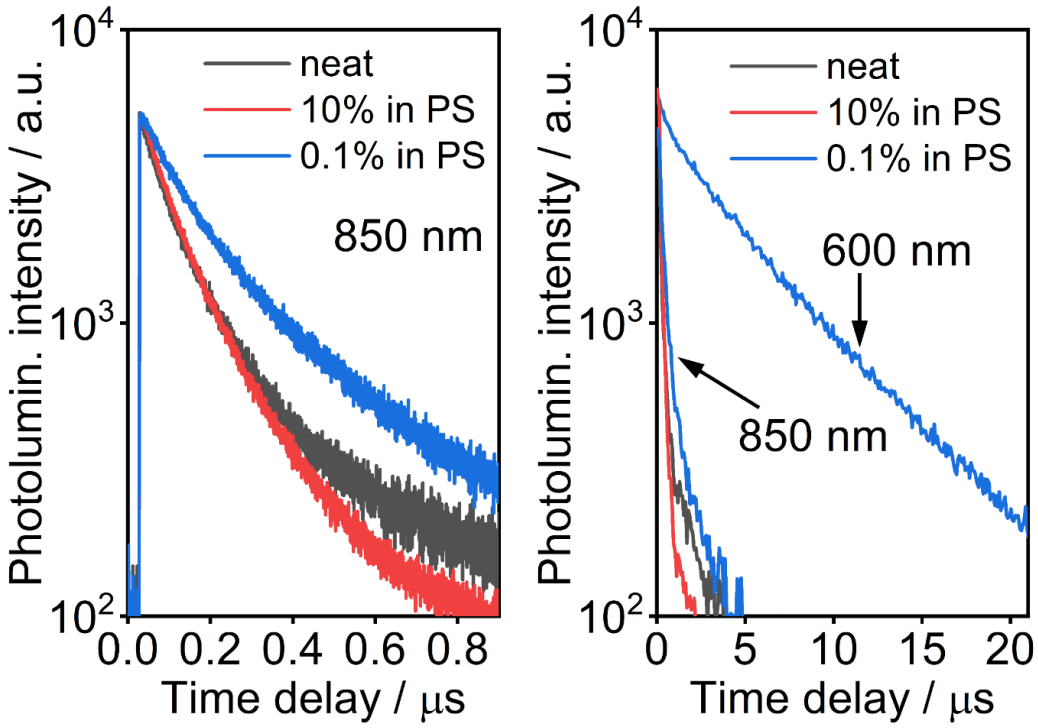

Figure S5.20. Photoluminescence decay traces of **2** in solid film (concentration in polystyrene, PS, or neat film indicated in figure legend). Left: decay of excimer emission at 850 nm; right: comparison of exciton (600 nm) and excimer (850 nm) decay. Note the exciton decay in 10% and neat film were not recorded due to low signal intensity.

e) Powder and crystal

Apart from studying **2** in film and solution, we have decided to look into the properties of the complex in powder and crystal. One important aspect of this study is to understand whether there are any intermolecular interactions present in bulk powder/crystals leading to formation of NIR-emissive excimers or dimers. We have studied the orange powder as obtained from the synthesis which shows orange-red luminescence at room temperature. We have also studied red crystals identical to those used for X-Ray diffraction analysis which show orange-red luminescence similar to the powder.

The most striking is the lack of any significant contribution of the excimer NIR band which can clearly be observed in film (**Figure S5.21**). The emission spectra are very similar to that of single molecules in a diluted solution, which indicates no significant intermolecular interactions leading to a bimolecular excited state. We remember a dominating excimer character of the emission in a solution-processed pristine film and in polymer matrix. We believe the films in question to be amorphous as per the way they are fabricated. A clear link between excimer properties in amorphous media and unimolecular emission in crystals can be drawn. One may hypothesize there to be less freedom for the molecules to migrate in the crystal than there is in amorphous phase. Molecules in a crystal would retain their position in the excited state which prevents excimer formation.

Overall, photoluminescent properties of **2** in powder and crystal resemble the behaviour in dilute polystyrene films. In both cases TADF is present at temperatures from 300 K down to 160-180 K (**Figure S5.23** and **Figure S5.24**). At temperatures below 160 K one can only observe phosphorescence in the photoluminescence spectrum. Photoluminescence lifetime in the temperature range from 300 K to 160 K can be fitted with equation 1 in the main text resulting in a similar estimated TADF activation energy, E_a, as in polystyrene film (**Figure S5.25** and **Figure S5.26**). Further increase of photoluminescence lifetime at temperature below 160 K can be attributed to non-radiative deactivation of the T_1 state.

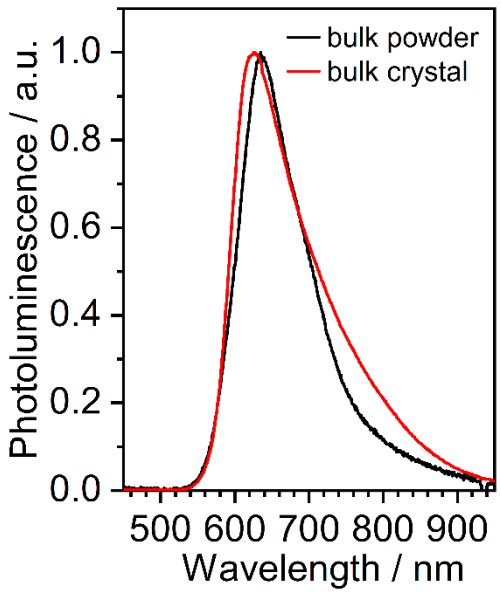

Figure S5.21. Photoluminescence spectra of **2** in crystal and powder at room temperature. Note contribution of excimer luminescence is negligible in both cases.

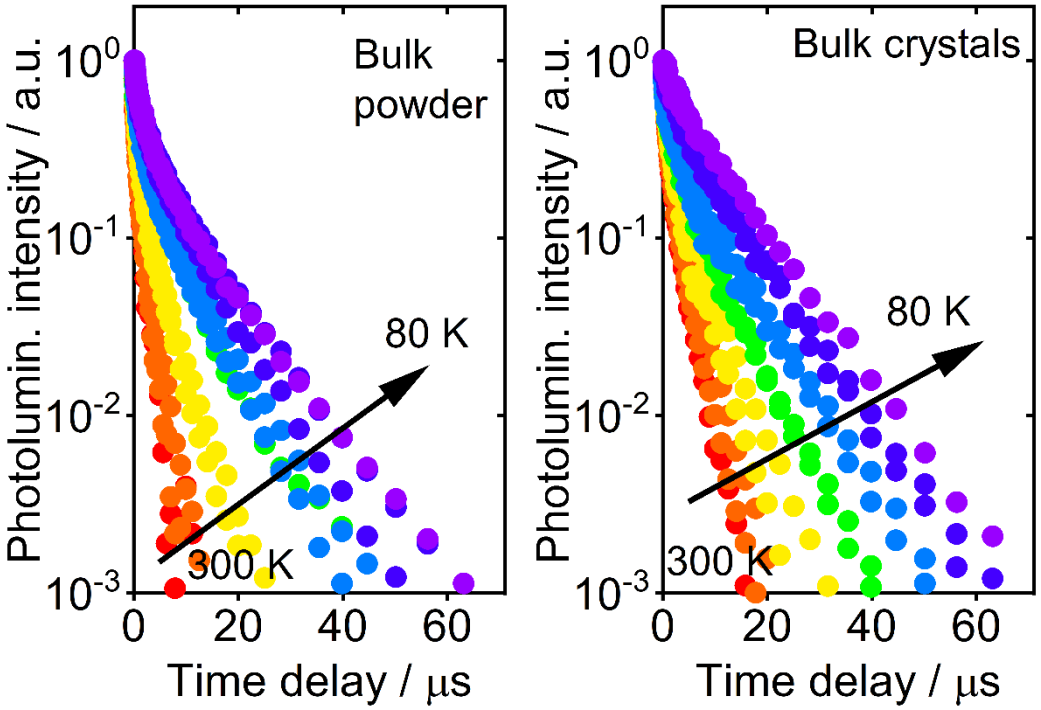

Figure S5.22. Photoluminescence decay of **2** in crystal and powder at various temperatures.

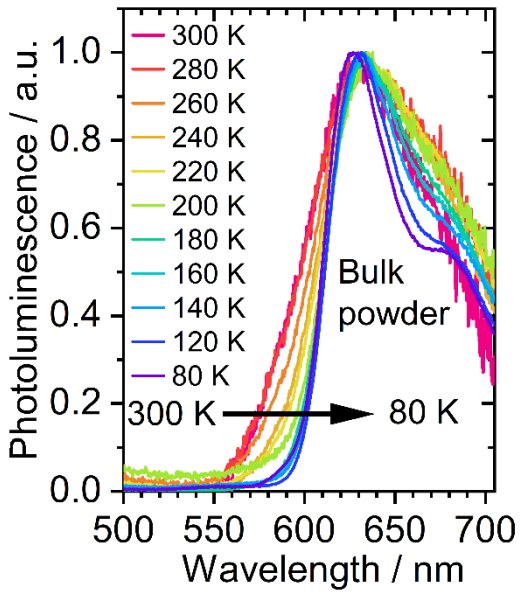

Figure S5.23. Photoluminescence spectra of **2** in powder at various temperatures.

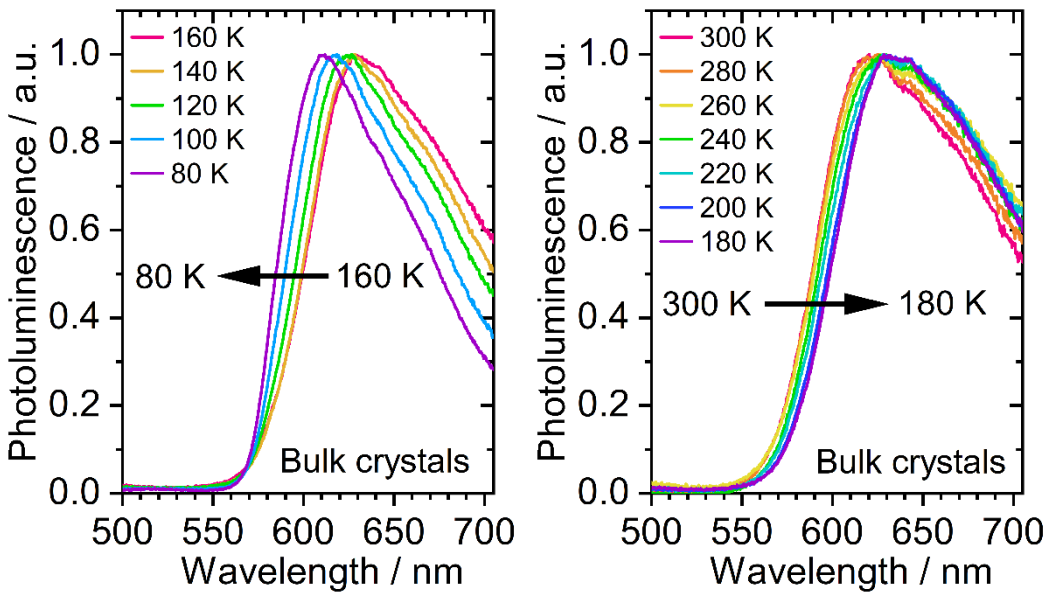

Figure S5.24. Photoluminescence spectra of **2** in crystal at various temperatures.

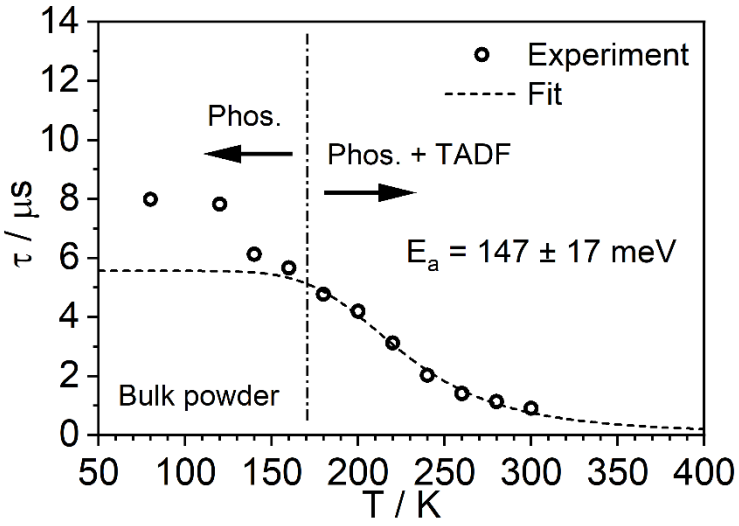

Figure S5.25. Photoluminescence decay lifetime of **2** in powder at various temperatures.

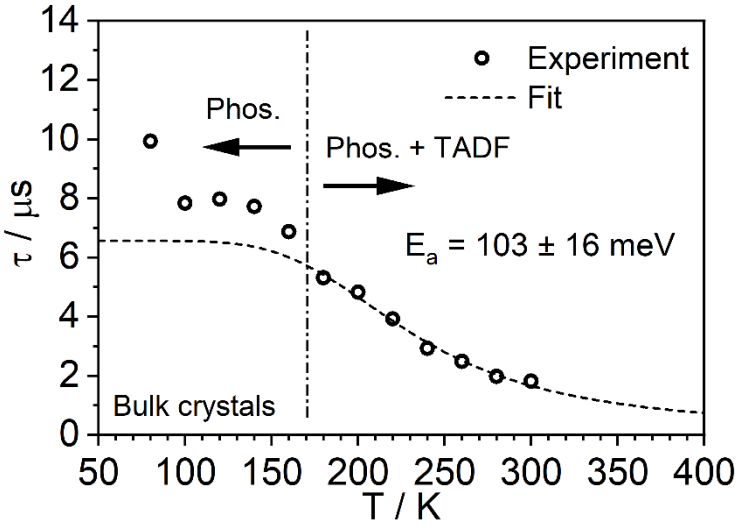

Figure S5.26. Photoluminescence decay lifetime of **2** in crystal at various temperatures.

6. Electrochemistry

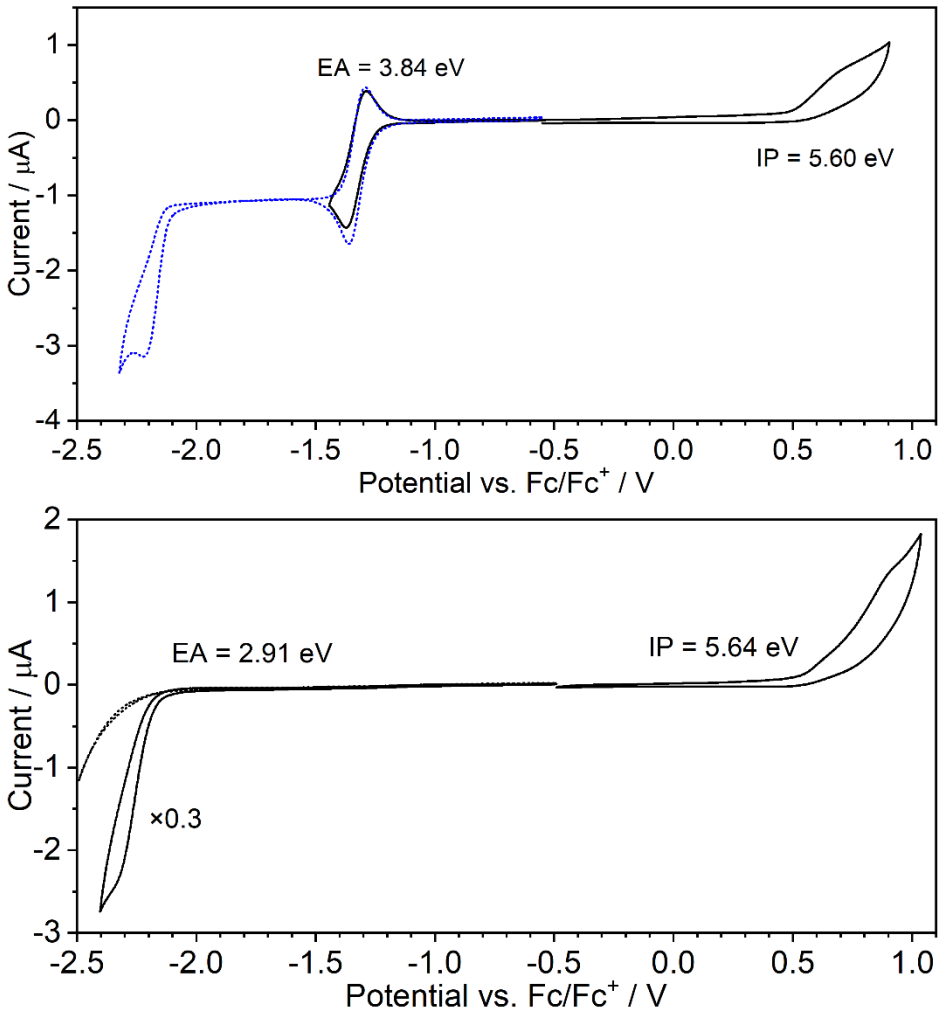

Figure S6.1 Cyclic voltammograms (CV) spectra of **2** (top) and **3** (bottom) at c = 10^{-3} M in 0.1 M Bu_4NBF_4 in CH_2Cl_2.

Electrochemical redox behaviour of **2** and **3** is typical for Pt(II) complexes (**Figure S6.1**). Both molecules undergo irreversible oxidation with similar onset potentials of 0.50 V and 0.54 V respectively *vs.* Fc/Fc^+ standard potential. **3** undergoes an irreversible reduction at very low onset potential of -2.19 V, which is close to the end of the electrochemical window of the electrolyte (black dotted line in the bottom graph indicates electrolyte redox response). Conversely, **2** shows a relatively shallow reversible reduction at -1.26 V onset with $E_{½}$ = -1.33 V and a second, irreversible reduction at -2.12 V onset. The second reduction process of **2** and **3** seem to occur at very similar potential (-2.19 V *vs.* -2.12 V), however this is likely a coincidence and these two values are not related. In **3** the process relates to accepting the first electron by a *neutral* molecule, while **2** it is a *second* reduction process where electron is injected into an anion.

Overall, the redox behaviour of both complexes stays in a good correlation with calculations: oxidation, being related to the HOMO, occurs at similar onset potential in both compounds. On the other hand, reduction takes place at clearly less negative potential in **2** as it does in **3** which is related to the significantly more electron deficient structure of ligand in the former. The additional electron is stabilised by the pyrimidine linker as shows the distribution of the LUMO orbital.

7. OLED devices

In addition to the OLED devices presented in the main text, we have also produced a device comprising neat **2** layer as the emissive layer. We believe the emitter acts as a poor electron transport layer and therefore, in the absence of a hole transporting host, recombination on emitter is marginal. For this reason it was impossible to record EQE or radiosity as them being too low. It was possible however to record an electroluminescence spectrum of the device, which is shown below.

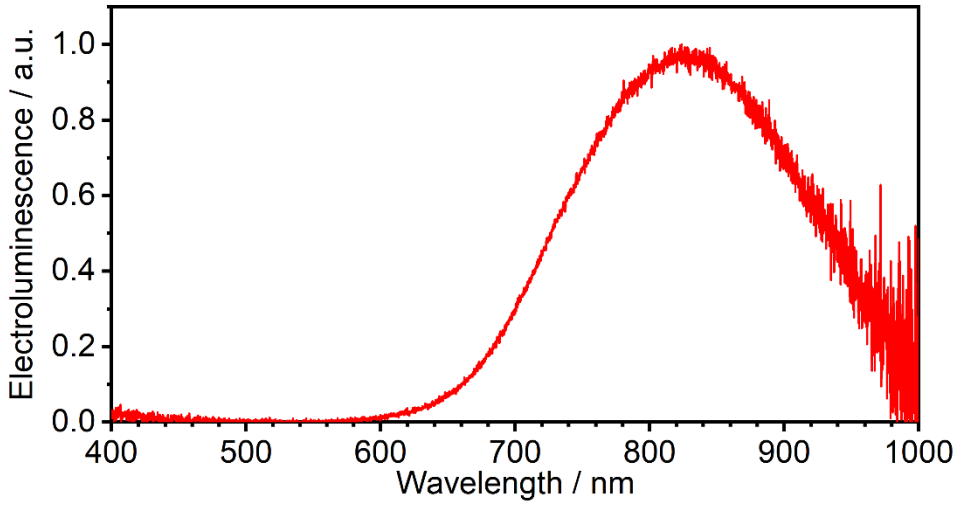

Figure S7.1 Electroluminescence spectrum of a device ITO | PEDOT:PSS Al4083 (30 nm) | **2** (≈30 nm) | PO-T2T (50 nm) | LiF (0.8 nm) | Al (100 nm). Note the λ_{el} = 824 nm.

Table S7.1 Compilation of reported NIR OLED efficiency ($\lambda_{el} \approx$ 700-1000 nm) of platinum(II) complexes. Note that solution-processed OLEDs are highlighted in light gray.

Emitter type	OLED fabrication method	λ_{el}, nm	EQE, %	Reference
Mono-Pt(II)	Solution-processed	1005	0.2	[25]
Mono-Pt(II)	Solution-processed	898	0.75	[25]
Di-Pt(II) excimer/aggregate	Solution-processed	805	0.51	THIS WORK
Mono-Pt(II)	Solution-processed	771	2.1	[25]
Di-Pt(II)	Solution-processed	746	0.56	[27]
Di-Pt(II)	Solution-processed	731	3.6	[26]
Excimer/aggregate	Solution-processed	716	5.1	[32]
Excimer/aggregate	Solution-processed	704	8.9	[31]
Excimer/aggregate	Solution-processed	700	8.1	[31]
Excimer/aggregate	Solution-processed	692	6.3	[31]
Excimer/aggregate	Thermal evaporation	930	2.0	[30]
Excimer/aggregate	Thermal evaporation	900	1.7	[30]
Mono-Pt(II)	Thermal evaporation	900	3.8	[25]
Mono-Pt(II)	Thermal evaporation	896	3.8	[24]
Excimer/aggregate	Thermal evaporation	890	2.1	[30]
Mono-Pt(II)	Thermal evaporation	773	8.0	[25]
Excimer/aggregate	Thermal evaporation	740	24	[29]
Excimer/aggregate	Thermal evaporation	724	16.7	[28]

8. References

[1] F. Neese, *WIREs Comput. Mol. Sci.* **2018**, *8*, DOI: 10.1002/wcms.1327.

[2] F. Neese, *WIREs Comput. Mol. Sci.* **2012**, *2*, 73.

[3] S. Lehtola, C. Steigemann, M. J. T. Oliveira, M. A. L. Marques, *SoftwareX* **2018**, *7*, 1.

[4] A.-R. Allouche, *J. Comput. Chem.* **2011**, *32*, 174.

[5] F. Weigend, R. Ahlrichs, *Phys. Chem. Chem. Phys.* **2005**, *7*, 3297.

[6] A. D. Becke, *J. Chem. Phys.* **1993**, *98*, 5648.

[7] P. J. Stephens, F. J. Devlin, C. F. Chabalowski, M. J. Frisch, *J. Phys. Chem.* **1994**, *98*, 11623.

[8] F. Weigend, *Phys. Chem. Chem. Phys.* **2006**, *8*, 1057.

[9] E. van Lenthe, E. J. Baerends, J. G. Snijders, *J. Chem. Phys.* **1993**, *99*, 4597.

[10] E. van Lenthe, E. J. Baerends, J. G. Snijders, *J. Chem. Phys.* **1994**, *101*, 9783.

[11] D. A. Pantazis, X. Y. Chen, C. R. Landis, F. Neese, *J. Chem. Theory Comput.* **2008**, *4*, 908.

[12] F. Neese, F. Wennmohs, A. Hansen, U. Becker, *Chem. Phys.* **2009**, *356*, 98.

[13] R. Izsák, F. Neese, *J. Chem. Phys.* **2011**, *135*, 144105.

[14] K. Nozaki, *J. Chinese Chem. Soc.* **2006**, *53*, 101.

[15] K. Mori, T. P. M. Goumans, E. van Lenthe, F. Wang, *Phys. Chem. Chem. Phys.* **2014**, *16*, 14523.

[16] P. Data, P. Pander, M. Lapkowski, A. Swist, J. Soloducho, R. R. Reghu, J. V. Grazulevicius, *Electrochim. Acta* **2014**, *128*, 430.

[17] P. Pander, P. Data, R. Turczyn, M. Lapkowski, A. Swist, J. Soloducho, A. P. Monkman, *Electrochim. Acta* **2016**, *210*, 773.

[18] C. M. Cardona, W. Li, A. E. Kaifer, D. Stockdale, G. C. Bazan, *Adv. Mater.* **2011**, *23*, 2367.

[19] J.-L. Bredas, *Mater. Horiz.* **2014**, *1*, 17.

[20] P. Pander, P. Data, F. B. Dias, *J. Vis. Exp.* **2018**, DOI: 10.3791/56614.

[21] D. de Sa Pereira, A. P. Monkman, P. Data, *J. Vis. Exp.* **2018**, DOI: 10.3791/56593.

[22] O. V. Dolomanov, L. J. Bourhis, R. J. Gildea, J. A. K. Howard, H. Puschmann, *J. Appl. Crystallogr.* **2009**, *42*, 339.

[23] G. M. Sheldrick, *Acta Crystallogr. Sect. A Found. Crystallogr.* **2008**, *64*, 112.

[24] J. R. Sommer, R. T. Farley, K. R. Graham, Y. Yang, J. R. Reynolds, J. Xue, K. S. Schanze, *ACS Appl. Mater. Interfaces* **2009**, *1*, 274.

[25] K. R. Graham, Y. Yang, J. R. Sommer, A. H. Shelton, K. S. Schanze, J. Xue, J. R. Reynolds, *Chem. Mater.* **2011**, *23*, 5305.

[26] M. Z. Shafikov, P. Pander, A. V. Zaytsev, R. Daniels, R. Martinscroft, F. B. Dias, J. A. G. Williams, V. N. Kozhevnikov, *J. Mater. Chem. C* **2021**, *9*, 127.

[27] K. Zhang, Y. Liu, Z. Hao, G. Lei, S. Cui, W. Zhu, Y. Liu, *Org. Electron.* **2020**, *87*, 105902.

[28] X. Yang, H. Guo, X. Xu, Y. Sun, G. Zhou, W. Ma, Z. Wu, *Adv. Sci.* **2019**, *6*, 1801930.

[29] K. Tuong Ly, R. W. Chen-Cheng, H. W. Lin, Y. J. Shiau, S. H. Liu, P. T. Chou, C. S. Tsao, Y. C. Huang, Y. Chi, *Nat. Photonics* **2017**, *11*, 63.

[30] Y.-C. Wei, S. F. Wang, Y. Hu, L.-S. Liao, D.-G. Chen, K.-H. Chang, C.-W. Wang, S.-H. Liu, W.-H. Chan, J.-L. Liao, W.-Y. Hung, T.-H. Wang, P.-T. Chen, H.-F. Hsu, Y. Chi, P.-T. Chou, *Nat. Photonics* **2020**, *14*, 570.

[31] W. Xiong, F. Meng, H. Tan, Y. Wang, P. Wang, Y. Zhang, Q. Tao, S. Su, W. Zhu, *J. Mater. Chem. C* **2016**, *4*, 6007.

[32] X. Wu, D.-G. Chen, D. Liu, S.-H. Liu, S.-W. Shen, C.-I. Wu, G. Xie, J. Zhou, Z.-X. Huang, C.-Y. Huang, S.-J. Su, W. Zhu, P.-T. Chou, *J. Am. Chem. Soc.* **2020**, *142*, 7469.